Boundary of nighttime ozone chemical equilibrium in the mesopause region: long-term evolution fromdetermined using 20-year satellite observations

Mikhail Yu. Kulikov[1], Mikhail V. Belikovich[1], Aleksey G. Chubarov[1], Svetlana O. Dementyeva[1], and Alexander M. Feigin[1]

[1]A. V. Gaponov-Grekhov Institute of Applied Physics of the Russian Academy of Sciences, 46 Ulyanov Str., 603950 Nizhny Novgorod, Russia

Correspondence to: Mikhail Yu. Kulikov (mikhail_kulikov@mail.ru)

Abstract. The assumption of nighttime ozone chemical equilibrium (NOCE) is widely ~~used~~employed for ~~retrieval of~~retrieving the O_x-HO_x components in the mesopause from rocket and satellite measurements. In this work, the recently developed analytical criterion of determining the NOCE boundary is ~~applied (1~~used (i) to study ~~of~~the connection of this boundary with O and H spatiotemporal variability ~~basing~~based on ~~the~~ 3D modeling of chemical transport~~ modeling~~, and (~~2~~ii) to retrieve and analyze the spatiotemporal evolution of the NOCE boundary in 2002-2021 from the SABER/TIMED data set. It was revealed, first, that the NOCE boundary ~~well~~ reproduces well the transition zone dividing deep and weak ~~diurnal~~ photochemical oscillations of O and H ~~at the low and middle latitudes~~caused by the diurnal variations of solar radiation. Second, the NOCE boundary is sensitive to sporadic abrupt changes in the middle atmosphere dynamics, in particular, due to powerful sudden stratospheric warmings leading to the events of an elevated (up to ~80 km) stratopause, which took place in January-~~February~~March 2004, 2006, 2009, 2010, 2012, 2013, 2018, and 2019. Third, the space-time evolution of this ~~characteristics~~characteristic expressed via pressure~~ height~~ altitude contains a clear signal of 11-year solar cycle in the ~~range of~~ 55ºS-55ºN range. In particular, ~~average~~the mean annual~~ the~~ NOCE boundary averaged in this range of latitudes anticorrelates well with $F_{10.7}$ index with the coefficient ~~of~~ -0.~~96~~95. Moreover, it shows a weak linear trend of ~~49~~the 56.2±~~36~~42.2 m/decade.

1 Introduction

The mesopause (80-100 km) is an interesting region of ~~Earth'~~the Earth's atmosphere possessing quite a number of unique phenomena and processes which can be considered as sensitive indicators/predictors of global climate change and anthropogenic influences on atmospheric composition (e.g., ~~(~~Thomas et al., 1989~~)).~~). Here, the summer temperature at middle and high latitudes~~ in the summer~~ reaches its lowest values (down to 100K (Schmidlin, 1992)). The temperatures below 150K lead to water vapour condensation and formation of the highest altitude clouds ~~on Earth~~in the Earth's atmosphere, the so-called Polar Mesospheric Clouds or Noctilucent Clouds~~,~~ consisting primarily of water ice (Thomas, 1991). In ~~opposite~~turn, the temperature of the winter mesopause is essentially higher, so there is a strong negative temperature gradient between the summer and winter hemispheres. At these altitudes, atmospheric waves ~~with~~of various spatiotemporal scales are observed, in particular, internal gravity waves coming from the lower atmosphere. Destruction of gravity waves leads to strong turbulence that affects the atmospheric circulation and ultimately manifests itself in the mentioned temperature structure of this region.

Many layer phenomena in the mesopause are ~~connected with~~related to the photochemistry of the O_x-HO_x components (O, O_3, H, OH, and HO_2). ~~Here, there~~There is a narrow (in height) transition region where photochemistry ~~behavior~~behaviour transforms rapidly from “deep” diurnal oscillations, when the difference between daytime and nighttime values of the O_x-HO_x components can ~~rich~~reach several orders of magnitude, to weak photochemical oscillations. As ~~the~~a result, above this region, ~~there takes place~~ O and H ~~accumulation and their~~accumulate to form the corresponding layers. This layer formation ~~manifesting~~manifests itself in the appearance of a secondary ozone maximum and airglow layers of OH and O excited states. Thus, O_x-HO_x photochemistry in the mesopause is responsible for the presence of important (first of all, from a practical point of view) indicators observed in the visible and infrared ranges, which are widely used for ground-based and satellite monitoring of climate changes and ~~waves~~wave activity. Moreover, O_x-HO_x photochemistry provides the total chemical heating rate of this region, influences the radiative cooling and other useful airglows (for example, by O_2 excited states), ~~involves~~is involved in the plasma-chemical reactions and formation of layers of the ionosphere ~~layers~~. The mentioned transformation of O_x-HO_x ~~behavior~~behaviour with height may ~~happens~~occur via the nonlinear response of O_x-HO_x photochemistry to the diurnal variations of solar radiation in the form of subharmonic (with periods of 2, 3, 4, and more days) or ~~the~~ chaotic oscillations (e.g., Sonnemann and Fichtelmann, 1997; Feigin et al., 1998). This unique phenomenon was predicted many years ago (~~e.g.,~~ Sonnemann and Fichtelmann, 1987) and investigated theoretically by models ~~with~~ taking into account ~~of~~ different transport processes (~~e.g.,~~ Sonnemann and Feigin, 1999; Sonnemann et al., 1999; Sonnemann and Grygalashvyly, 2005; Kulikov and Feigin, 2005; Kulikov, 2007; Kulikov et al., 2020). It was revealed, in particular, that the ~~appearance of~~ nonlinear response is controlled by ~~the~~ vertical eddy diffusion (Sonnemann and Feigin, 1999; Sonnemann et al., 1999), so that 2-day oscillations can only survive at ~~the~~ real diffusion coefficients, but the eddy diffusion in zonal direction leads to the appearance of the so-called reaction-diffusion waves in the form of propagating phase fronts of 2-day oscillations (Kulikov and Feigin, 2005; Kulikov et al., 2020). Recently, the satellite data processing ~~found~~revealed the first evidence ~~that~~of the existence of 2-day photochemical oscillations ~~exist~~ in the real mesopause (Kulikov et al., 2021).

While regular remote sensing measurements of most O_x-HO_x components are still limited, the indirect methods based on the physicochemical assumptions are useful tools ~~to monitor~~for monitoring these trace gases. In many papers, ~~the~~ O and H distributions were retrieved from the daytime and nighttime rocket and satellite measurements of the ozone and the volume emission rates of OH(ν), $O(^1S)$, and $O_2(a^1\Delta_g)$ (~~e.g.,~~ Good, 1976; Pendleton et al., 1983; McDade et al., 1985; McDade and Llewellyn, 1988; Evans et al., 1988; Thomas, 1990; Llewellyn et al., 1993; Llewellyn and McDade, 1996; Mlynczak et al., 2007, 2013a, 2013b, 2014, 2018; Smith et al., 2010; Xu et al., 2012; Siskind et al., 2008, 2015). The retrieval technique is based on the assumption of ~~the~~ ozone photochemical/chemical equilibrium and physicochemical model of the corresponding airglow, which describe the ~~relations~~relationship between local O and H values and ~~the~~ measurement data.

The daytime photochemical ozone equilibrium is a good approximation everywhere in the mesosphere ~~-~~ – lower thermosphere (MLT) region (Kulikov et al., 2017) due to ozone photodissociation, whereas the applicability of the assumption of nighttime ozone chemical equilibrium (NOCE) is limited: there is an altitude boundary ~~upper~~above which NOCE is satisfied ~~with~~to an accuracy better than 10%. Below this boundary, the ozone equilibrium is disturbed essentially and cannot be used. Good (1976) supposed that NOCE is fulfilled above 60 km, whereas other papers apply the NOCE starting from 80 km, independent of latitude and season. However, studies of NOCE within the framework of the 3D chemical-transport models (Belikovich et al., 2018; Kulikov et al., 2018a) revealed that the NOCE boundary ~~of NOCE~~ varies within the range of 81–87 km, depending on latitude and season. ~~Due to~~In view of the practical ~~necessity~~need to determine the local altitude position of this boundary, Kulikov et al. (2018a) presented a simple criterion ~~localizing of~~determining the equilibrium boundary using only the data provided by the SABER (Sounding of the Atmosphere using Broadband Emission Radiometry) instrument onboard the TIMED (Thermosphere Ionosphere Mesosphere Energetics and Dynamics). ~~Using~~Making use of this criterion, Kulikov et al. (2019) retrieved the annual evolution of the NOCE boundary from the SABER data. It was revealed that ~~the~~a two-month averaged NOCE boundary essentially depends on season and latitude and can rise up to ~ 86 km. Moreover, the analysis of the NOCE boundary in 2003-2005 showed that this characteristic was sensitive to unusual dynamics of stratospheric polar vortex during the 2004 Arctic winter ~~2004~~, which was named ~~as~~a remarkable winter in the 50-year record of meteorological analyses (Manney et al., 2005). Moreover, Belikovich et al. (2018) found by 3D simulation that the excited OH layer ~~well~~ repeats well spatiotemporal variability of the NOCE boundary. These results ~~let~~allowed us to speculate that the NOCE boundary can be considered as an important indicator of ~~mesopause'~~mesopause processes.

The main goals of this paper are (1) to investigate the ~~connection of~~relationship between the NOCE boundary according to the mentioned criterion ~~with~~and O and H variability with the use of the 3D chemical transport model, and (2) to retrieve and analyze the spatiotemporal evolution of the NOCE boundary in 2002-2021 from the SABER/TIMED data set. In the next section, we present the used model. In Section 3, we briefly describe ~~shortly~~ the criterion ~~to determine~~of determining the NOCE boundary local height and study how this height ~~relates with~~is related to the features of O and H distributions from the 3D model. Section 4 explains the methodology of determining the NOCE boundary from satellite data. Section 5 presents the main results obtained from SABER/TIMED data~~, which are~~ discussed in Section 6.

2 3D model

We use the 3D chemical transport model of the middle atmosphere developed by the Leibniz Institute of Atmospheric Physics (~~e.g., ~~Sonnemann et al., 1998; Körner and Sonnemann, 2001; Grygalashvyly et al., 2009; Hartogh et al., 2004, 2011). The three-dimensional fields of temperature and winds were adopted by Kulikov et al. (2018b) from the Canadian Middle Atmosphere Model (Scinocca et al., 2008) for the year 2000 with an updated frequency of 6 hours. To exclude unrealistic jumps in the evolution of calculated chemical characteristics, ~~a ~~linear smoothing between two subsequent updates of these parameters is applied. The model takes into account 3D advective transport and vertical diffusive transport (both, turbulent and molecular). The Walcek-scheme (Walcek, 2000) and the implicit Thomas algorithm (Morton and Mayers, 1994) are used for advective and diffusive transport, respectively. The model grid includes 118 pressure-height levels (from the ground to ~135 km), 32 and 64 levels in latitude and longitude, respectively. The chemical part considers 22 constituents (O, O(^{1}D), O_3, H, OH, HO_2, H_2O_2, H_2O, N, NO, NO_2, NO_3, N_2O, CH_4, CH_2, CH_3, CH_3O_2, CH_3O, CH_2O, CHO, CO, CO_2), 54 two- and three-body reactions, and 15 photo-dissociation reactions. The model uses pre-calculated ~~dependencies~~dependences of dissociation rates on ~~the ~~altitude and solar zenith angle (Kremp et al., 1999). ~~For the~~The chemistry ~~calculation, we apply~~is calculated by the Shimazaki scheme (Shimazaki, 1985) ~~at~~for the integration time of 9 sec.

3 The NOCE criterion

The nighttime ozone chemistry at the mesopause heights is determined mainly by two reactions R1-R2 (e.g., Allen et al., 1984), see Table 1. ~~Thus,~~The secondary ozone loss via the O + $O_3 \rightarrow 2O_2$ reaction becomes important above ~ 95 km (Smith et al., 2009). Kulikov et al. (2023) verified with simulated and measured data that this reaction does not influence the NOCE boundary determination and may be skipped. Thus, the ozone equilibrium concentration ($O_3{}^{eq}$) corresponding to the instantaneous balance between the production and loss terms is as follows:

$$O_3{}^{eq} = \frac{k_1 \cdot O \cdot O_2 \cdot M}{k_2 \cdot H}, \quad (1)$$

where M is air concentration, and k_{1-2} are the corresponding rate constants of the reactions (see Table 1).

As mentioned above, the NOCE criterion was developed in Kulikov et al. (2018a). The main idea is that the local values of O_3 and $O_3{}^{eq}$ are close ~~to each other ~~($O_3(t) \approx O_3{}^{eq}(t)$), when $\tau_{O_3} \ll \tau_{O_3{}^{eq}}$, where τ_{O_3} is the ozone lifetime and $\tau_{O_3{}^{eq}}$ is the local time scale of $O_3{}^{eq}$:

$$\tau_{O_3} = \frac{1}{k_2 \cdot H}, \qquad (2)$$

$$\tau_{O_3{}^{eq}} \equiv \frac{O_3{}^{eq}}{|dO_3{}^{eq}/dt|} = \frac{O}{H \cdot \left|\frac{d}{dt}\left(\frac{O}{H}\right)\right|}. \qquad (3)$$

As shown in Kulikov et al. (2018a), $\tau_{O_3{}^{eq}}$ can be determined from a simplified photochemical model describing the O_x-HO_x evolution in the mesopause region (Feigin et al., 1998), so the criterion ~~for validity~~ of the NOCE validity can be written in the form:

$$Cr = \frac{\tau_{O_3}}{\tau_{O_3{}^{eq}}} = 2\frac{k_1 \cdot k_4 \cdot O_2{}^2 \cdot M^2}{k_2}\left(1 - \frac{k_5 + k_6}{k_3}\right) \cdot \frac{1}{k_2 \cdot H \cdot O_3} \ll 1, \qquad (4)$$

where k_i are the corresponding reaction constants from Table 1. Calculations with the global 3D chemistry-transport model of the middle atmosphere showed (Kulikov et al. 2018a) that the criterion $\tau_{O_3}/\tau_{O_3{}^{eq}} \leq 0.1$ ~~well~~ defines well the boundary of the area where $|O_3/O_3{}^{eq} - 1| \leq 0.1$.

Kulikov et al. (2023) presented the theory of chemical equilibrium of a certain trace gas n. Strictly mathematically, the cascade of ~~the~~ sufficient conditions for $n_i(t) \cong n_i{}^{eq}(t)$ was derived considering its lifetime, equilibrium concentration, and time dependences of these characteristics. In case of the nighttime ozone, it was proved that ~~the~~ $\tau_{O_3}/\tau_{O_3{}^{eq}} \ll 1$ is the main condition for NOCE validity and the criterion $\tau_{O_3}/\tau_{O_3{}^{eq}} \leq 0.1$ limits ~~the~~a possible difference between O_3 and $O_3{}^{eq}$ to ~~be no~~not more than ~10%. Moreover, Kulikov et al. (2023) slightly corrected the expression for the criterion (4):

$$\mathrm{Cr} = 2\frac{k_1 \cdot O_2 \cdot M}{k_2}\left(k_4 \cdot M \cdot O_2 \cdot \left(1 - \frac{k_5 + k_6}{k_3}\right) + k_2 \cdot O_3\right) \cdot \frac{1}{k_2 \cdot H \cdot O_3} \leq 0.1. \qquad (5)$$

~~Other~~One more important condition for $O_3 \approx O_3{}^{eq}$ at the time moment t is:

$$e^{\int_{t_{bn}}^{t} \tau_{O_3}{}^{-1} dt} \gg 1, \qquad (6)$$

where t_{bn} is the time of the beginning of the night. ~~It means the nighttime data measured near the~~ The ozone equilibrium concentration jumps at sunset ~~should be excluded from consideration~~due to the shutdown of photodissociation. Thus, the condition (6) shows that it takes time for the ozone concentration to reach a new equilibrium. Kulikov et al. (2023) revealed that, at the solar zenith angle $\chi > 95°$, the condition (6) is fulfilled ~~in~~ almost in all cases, and the condition (5) becomes the main criterion for NOCE validity. In addition, Kulikov et al. (2023) demonstrated with the use of a 3-D model that the criterion (5) almost ideally reproduces the NOCE boundary found by direct comparison of O_3 and $O_3{}^{eq}$ concentrations, see Figure 1 in Kulikov et al. (2023).

Figures 1-3 demonstrate model examples of O and H time-height variations above different points ~~in~~over three months. In order to focus ~~our~~ attention on diurnal oscillations, the concentrations are normalized by mean daily values, ~~correspondingly~~which were calculated as a function of altitude. These daily average O and H values were different for each altitude. One can see in all panels of these ~~Figures, first, below 81-87 km,~~figures ”deep” diurnal oscillations that occur below 81-87 km. Due to the shutdown of sources at night and high rates of the main HO_x and O sinks nonlinearly dependent on air concentration (Konovalov and Feigin, 2000), the variables change during each night within ~~a~~the range of several orders of magnitude with low values of ~~times~~time evolution. Above 83-88 km, the situation differs essentially from the previous case. One can see ~~the~~ relatively weak diurnal oscillations. These regimes of O and H ~~behavior~~behaviour are ~~in~~ consistent ~~each other~~, i.e. deep H diurnal oscillations correspond to the same dynamics in O, and so on. There exists a few~~-~~-km thick layer (transition zone) dividing deep and weak oscillations ~~which~~whose height position ~~is depended~~depends on latitude and season. In particular, in summer the middle latitude transition is higher than in winter. Figures 1-3 show also the magenta lines pointing the NOCE boundary in accordance ~~to~~with the criterion (5) (Cr = 0.1). One can see that the NOCE criterion almost perfectly reproduces the features of the transition zone. Thus, our criterion is not only ~~the~~a useful technical characteristic to retrieve O from satellite data, but it also points ~~the~~to an important dynamical process in the O_x-HO_x photochemistry.

4 ~~Boundary of the~~ NOCE boundary from satellite data

We use ~~the~~ version 2.0 of the SABER data product (Level2A) for the simultaneously measured ~~height~~ profiles of pressure (p), altitude (z), temperature (T), O_3 (at 9.6 μm), and total volume emission rates of OH* transitions at 2.0 (VER) within the 0.0001–0.02 mbar pressure interval (altitudes approximately 75–105 km) in 2002-2021. We consider only nighttime data when the solar zenith angle $\chi > 95°$.

Kulikov et al. (2018a) noted that the term $k_2 \cdot H \cdot O_3$ in the expression for the NOCE criterion can be rewritten in the form ~~depended~~depending on measurable characteristics only with the use of the corresponding OH(v) model by Mlynczak et al. (2013a):

$$k_2 \cdot H \cdot O_3 = VER/A(T,M,O), \quad (7)$$

where $A(T,M,O)$ is ~~a~~the function in square brackets ~~of equation~~in Eq. (3) in the paper by Mlynczak et al. (2013a) with the parameters corrected by Mlynczak et al. (2018):

$A(T,M,O) =$ ~~$0.47 \cdot 118.35/(215.05 + 2.5 \cdot 10^{-11} \cdot O_2 + 3.36 \cdot 10^{-13} \cdot e^{220/T} \cdot N_2 + 3 \cdot 10^{-10} \cdot O) + 0.34 \cdot 117.21/(178.06 + 4.8 \cdot 10^{-13} \cdot O_2 + 7 \cdot 10^{-13} \cdot N_2 + 1.5 \cdot 10^{-10} \cdot O) + 0.47 \cdot 117.21/(215.05 + 2.5 \cdot 10^{-11} \cdot O_2 + 3.36 \cdot 10^{-13} \cdot e^{220/T} \cdot N_2 + 3 \cdot 10^{-10} \cdot O) \cdot (20.05 + 4.2 \cdot 10^{-12} \cdot O_2 + 4 \cdot 10^{-13} \cdot N_2)/(178.06 + 4.8 \cdot 10^{-13} \cdot O_2 + 7 \cdot 10^{-13} \cdot N_2 + 1.5 \cdot 10^{-10} \cdot$~~

~~O).~~ $$\frac{0.47\cdot118.35}{215.05+2.5\cdot10^{-11}\cdot O_2+3.36\cdot10^{-13}\cdot e^{\frac{220}{T}}\cdot N_2+3\cdot10^{-10}\cdot O}+\frac{0.34\cdot117.21}{178.06+4.8\cdot10^{-13}\cdot O_2+7\cdot10^{-13}\cdot N_2+1.5\cdot10^{-10}\cdot O}+$$

$$\frac{0.47\cdot117.21\cdot(20.05+4.2\cdot10^{-12}\cdot O_2+4\cdot10^{-13}\cdot N_2)}{(215.05+2.5\cdot10^{-11}\cdot O_2+3.36\cdot10^{-13}\cdot e^{\frac{220}{T}}\cdot N_2+3\cdot10^{-10}\cdot O)\cdot(178.06+4.8\cdot10^{-13}\cdot O_2+7\cdot10^{-13}\cdot N_2+1.5\cdot10^{-10}\cdot O)}. \quad (8)$$

This function is the result of the combination of the equations of physicochemical OH* balance in the v = 8 and v = 9 states. It depends on the constants of the processes describing sources and sinks ~~on~~at the corresponding levels, in particular, the OH(v) removal ~~in~~on collisions with O_2, N_2, and O. Below 86-87 km, $A(T,M,O) \cong A(T,M,O=0) \equiv A(T,M)$ ~~because of~~due to relativity small O concentrations. Thus, by combining Eqs. (5) and (7), the NOCE criterion for SABER data can be recast in the following form:

$$VER \geq VER_{min}(T,M) = 20\cdot\frac{k_1\cdot O_2\cdot M}{k_2}\left(k_4\cdot O_2\cdot M\cdot\left(1-\frac{k_5+k_6}{k_3}\right)+k_2\cdot O_3\right)\cdot A(T,M). \quad ~~(8)~~ (9)$$

Due to the strong air~~-~~ concentration~~-~~ dependence~~,~~ VER_{min} decreases rapidly with height. In particular, at 105 km, $VER \gg VER_{min}$. At 75 km, the relationship is ~~the~~ inverse. We determine the local position of the NOCE boundary (pressure level ~~p_{eq}~~$p_{eq}{}^{l}$ and altitude level ~~z_{eq}~~$z_{eq}{}^{l}$) according to the criterion (~~8~~9), where $VER = VER_{min}(T,M)$. We ~~carried out special verification~~verified that the approximation $A(T,M,O) \cong A(T,M)$ is valid near the NOCE boundary. With the use of annual SABER data, we calculated simultaneous datasets of $A(T,M)$ and $A(T,M,O)$. In the second case, we used O retrieved ~~O~~ from the same SABER data. The maximum and mean differences between $A(T,M)$ and $A(T,M,O)$ were found to be ~ 2% and ~ 0.1%, respectively.

The total range of latitudes according to the satellite trajectory over a month ~~is~~was ~(83.5°S - 83.5°N). This range was divided into 20 bins and all ~~single~~local values of ~~p_{eq}~~$p_{eq}{}^{l}$ and ~~z_{eq}~~$z_{eq}{}^{l}$ falling into one bin during a month or a year were averaged, respectively. ~~For convenience,~~ In particular, several thousand values of $p_{eq}{}^{l}$ and $z_{eq}{}^{l}$ fall into one bin during a month. Following Mlynczak et al. (2013a), averages were determined by binning the data of a certain day by local hour and then averaging over the hour bins that contain data to obtain the daily average value. Then we calculated monthly mean values of ~~p_{eq}~~$p_{eq}{}^{m}$ and $z_{eq}{}^{m}$ and annually mean values of $p_{eq}{}^{y}$ and $z_{eq}{}^{y}$ (hereafter, the indexes «m» and «y» indicate the monthly and annually average, respectively). Then, for convenience, the values of $p_{eq}{}^{m}$ and $p_{eq}{}^{y}$ were recalculated into the pressure ~~heights (pseudoheights) $z_{eq}{}^{pa}$~~ altitudes $h_{eq}{}^{m}$ and $h_{eq}{}^{y}$. The dependence of ~~$z_{eq}{}^{pa}$~~$h_{eq}{}^{m,y}$ on ~~the pressure~~$p_{eq}{}^{m,y}$ was ~~taken~~adopted from Mlynczak et al. (2013a, 2014~~).~~):

$$h_{eq}{}^{m,y} = -H_a\cdot\log\left(p_{eq}{}^{m,y}/p_0\right),\ H_a = 5.753474,\ p_0 = 11430.49428\ \text{hPa}. \quad (10)$$

Note that the use of both, geometrical and pressure coordinates is a rather common approach when analyzing long-term evolution of the obtained data, especially, when the data is the result of averaging over time and space. In particular, Lübken et al. (2013) demonstrated the importance of distinguishing between trends on pressure and geometrical altitudes in the mesosphere, since the second includes the atmospheric shrinking effect and is more pronounced. Grygalashvyly et al. (2014) analyzed the linear trends in OH* peak height and revealed a remarkable decrease at geometrical altitudes, which is almost absent at pressure altitudes.

Kulikov et al. (2023) studied the systematic uncertainty of the retrieved NOCE boundary height. Following the typical analysis presented, for example, in Mlynczak et al. (2013a, 2014), the uncertainty was obtained by calculating the root-sum-square of the individual sensitivity of the retrieved ~~characteristics~~characteristic to the perturbation of O_3, T, rates of reactions, and parameters of the *A* function. The systematic error of ~~z_{eq}^{pa}~~NOCE pressure altitude h_{eq}^{m} and ~~z_{eq} varies~~geometrical altitude z_{eq}^{m} varied in the range of 0.1-0.3 km, whereas the random error ~~is~~was negligible due to averaging ~~in~~over time and space.

5 NOCE boundary in 2002-2021 from SABER/TIMED data: main results

~~Figures~~Figure 4~~-7 demonstrate~~ demonstrates the ~~contour map of space-~~time evolution of ~~pseudoheight z_{eq}^{pa}~~the pressure altitude h_{eq}^{m} in 2002-2021 ~~and examples of z_{eq}^{pa} time evolution,~~in all latitude bins. Figures 5 (left column) show the mean (for 2002-2021) annual cycle ~~and~~of h_{eq}^{m} at four specific latitudes and Figures 6 (left column) present the Fourier spectra at ~~different~~these latitudes~~. It can be seen~~ obtained from the data in Figure 4. Note, first, that above ~~~55ºS~~58ºS,N, there are data gaps ~~due to~~specified by the satellite sensing geometry. For example, in 2002-2014, at 66.8-75.15°S,N ~~in 2002-2014,~~ measurements ~~cover~~covered 6 months per year only. In 2015, because of slight ~~change~~changes in the satellite geometry, there appeared additional months~~ appeared~~. This is especially noticeable above ~66ºS,N and manifests itself by extension of the variation range of ~~z_{eq}^{pa}~~h_{eq}^{m} at these latitudes in 2015-2021. Second, the variation range of ~~z_{eq}^{pa}~~h_{eq}^{m}, annual cycle and spectrum of harmonic oscillations ~~depend~~depends essentially on the latitude. Near the equator, ~~z_{eq}^{pa}~~h_{eq}^{m} varies in the 81-83 km range mainly and there are two main harmonics with periods of 1/2 and 1 year in the spectrum. At low latitudes, the variation range of ~~z_{eq}^{pa}~~h_{eq}^{m} narrows down to a minimum (~82~~.2~~-83~~.2~~ km at 16.7-20.05°S,N~~) that~~), which is accompanied ~~by~~with the appearance of a wide spectrum of harmonics with periods of 1/5, 1/4, 1/3, 1/2, and 1 year. At middle latitudes, the range of ~~z_{eq}^{pa}~~h_{eq}^{m} variation monotonically increases up to ~81.5-85.5 km with latitude and the harmonic with a period of 1 year becomes the main mode in the spectrum of oscillations. At both, low and middle latitudes, there is no signal from quasi-biennial oscillations but one can see a remarkable amplitude of a harmonic with a period of ~10 years, which can be associated with a manifestation of 11-year solar cycle.~~ Note~~ It is interesting that the mentioned features are typical for both hemispheres. At high latitudes, ~~$z_{eq}{}^{pa}$~~ $h_{eq}{}^{m}$ varies in the range of 79-86.5 km. At these latitudes, ~~it~~one can ~~seen~~see the main difference between ~~north~~the northern and ~~south~~southern hemispheres: the sharp falls and rises of the ~~north~~northern boundary of NOCE by several km (up to 3-4 km) appearing in January-~~February~~March 2004, 2006, 2009, 2010, 2012, 2013, 2018 and 2019 ~~and absenting~~that are absent at ~~south~~southern latitudes.

~~Analyzing the Figure 6, one can note~~The analysis of Figures 5-6 demonstrates the following redistribution in the annual cycle with increasing latitude from equator to polar latitudes. Near the equator, the annual cycle has two maxima in June – July and in December – January. The first one is more pronounced. That is why there are two main harmonics with periods of 1/2 and 1 year in the spectrum. At low latitudes, one maximum (summer) ~~remains in place, and~~does not change, while the other ~~begins to approach~~approaches the first one. As ~~the~~a result, the ~~wide~~ spectrum of harmonics ~~takes place~~is wide. At middle latitudes, the maxima gradually merge so that the 1 year-harmonic becomes the main one.

~~Figures 8-9 demonstrate the~~ Figure 7 (left) demonstrates a contour map of the space-time evolution of the average annual ~~$z_{eq}{}^{pa}$ ($< z_{eq}{}^{pa} >$, hereafter, the angle brackets are used to denote the values averaged in time and space)~~pressure altitude $h_{eq}{}^{y}$ in 2002-2021~~ and examples of ~~. Figure 8 presents the time evolution of this characteristic at different latitudes. ~~Basing~~Based on ~~Fourier's~~the Fourier spectra presented in ~~Figure 7,~~Figures 6 (left column), we can suppose that, at low and middle latitudes, the interannual variation of ~~$< z_{eq}{}^{pa} >$~~ $h_{eq}{}^{y}$ is caused by the 11-year solar cycle mainly. Figure ~~10~~9 (left) presents the correlation coefficient of ~~$< z_{eq}{}^{pa} >$~~ $h_{eq}{}^{y}$ with $F_{10.7}$ index (solar radio flux at 10.7 cm, see the red curve in Figure ~~8~~10) as a function of latitude. One can see good anticorrelation (with a coefficient from -0.~~74~~72 to -0.~~9~~92) between ~55ºS and ~55ºN. At high latitudes, the absolute value of the correlation coefficient decreases sharply ~~up~~down to ~0.~~56~~58 in the south and to ~0.1 in the north. ~~Blue~~The blue curve in Figure ~~11~~10 shows latitude-averaged ~~$< z_{eq}{}^{pa} >$~~ $h_{eq}{}^{y}$ in the range of 55ºS-55ºN. In this case, the anticorrelation with $F_{10.7}$ index is close to ideal (coefficient ~ -0.~~96~~95).

With the use of multiple linear regression in the 55ºS-55ºN range:

~~$< z_{eq}{}^{pa} > ($~~ $h_{eq}{}^{y}(year) = const + \alpha \cdot year + \beta \cdot F_{10.7}(year),$ (~~9~~11)

we determined a slow (up to 10 m/year) linear trend ~~in $< z_{eq}{}^{pa} >$~~of $h_{eq}{}^{y}$ as a function of latitude~~ in the range of 55ºS-55ºN (see Figure 12). One can see a tendency to increase $< z_{eq}{}^{pa} >$ at most latitudes with trend up to 10 m/year~~, but with ~~high uncertainty~~the uncertainties essentially larger than the trend values.

Applying the regression analysis to latitude-averaged $<z_{eq}^{pa}>$ $h_{eq}{}^{y}$ (blue curve in Figure 11) gives10) gave us a more statistically significant value of the trend: 4.92±35.62±4.22 m/year.

Figures 13-16 demonstrateFigure 11 demonstrates the contour map of space time evolution of realthe geometrical altitude of NOCE boundary$z_{eq}{}^{m}$ in 2002-2021, examples of z_{eq} time evolution, in all latitude bins. Figures 5 (right column) show the mean (for 2002-2021) annual cycle and of $z_{eq}{}^{m}$ at four specific latitudes and Figures 6 (right column) present the Fourier spectra at differentthese latitudes. Comparing obtained from the data in Figure 11. Comparison with Figures 4-7, it can be seen, first, z_{eq} and 5-6 (left columns) shows that $z_{eq}{}^{m}$ repeats many qualitative features of the space-time evolution of z_{eq}^{pa}pressure altitude $h_{eq}{}^{m}$. In particular, in the direction from the equator to the poles, the variation range of $z_{eq}$$z_{eq}{}^{m}$ first decreases updown to 1 km at 16º-25ºS,N, and then expandingexpands to several km at middle and high latitudes. In Figure 15, oneOne can see the same redistribution of the annual cycle with latitude, as it was mentioned in Figure 6similarly to the pressure altitude case. Near the equator, the annual cycle possesses two maxima occurring in June – July and in December – January. At low latitudes, one maximum continues to be in summer, whereas the other shifts into theto spring. At middle latitudes, the maxima gradually coalesce forming a single summer maximum. At north high northern latitudes, there are the same local sharp variations of the NOCE boundary in January-February 2004, 2006, 2009, 2010, 2012, 2013, 2018 and 2019, which are absent at southsouthern latitudes. Second One can see from Figure 5 that, on the average, $z_{eq}$$z_{eq}{}^{m}$ is lower than z_{eq}^{pa}. The difference $z_{eq}^{pa} - z_{eq}$ varies in the range of 0 – 1.5 km at equator, 0 – 2.5 km at 50º-58ºS,N and 1-4 km at 75º-83ºS,N. The maxima and minima of $z_{eq}^{pa} - z_{eq}$ are reached in winter and summer, respectively. In general, the variation range of z_{eq} during the year is wider$h_{eq}{}^{m}$ by about 10.5-41 km, depending on latitude. Third, theOne can see from Figure 6 that the $z_{eq}{}^{m}$ spectra of harmonic oscillations are similar to $z_{eq}^{pa}$the $h_{eq}{}^{m}$ spectra except for nothe absence of a signal of the 11-year solar cycle.

Figures 17-18 demonstrate the Figure 7(right) demonstrates a contour map of space-time evolution of the annually average annual z_{eq} ($<z_{eq}>$)geometrical altitude $z_{eq}{}^{y}$ in 2002-2021 and examples of . Figure 12 presents the time evolution of this characteristicscharacteristic at different latitudes. One can see, at all latitudes, that there is no clear evidence of 11-year solar cycle manifestation at all latitudes. This is confirmed by the calculation of the correlation coefficient of $<z_{eq}>$ $z_{eq}{}^{y}$ with $F_{10.7}$ index as a function of latitude (see Figure 19).9 (right)). Moreover, the latitude-averaged (in the range of 55ºS-55ºN) $<z_{eq}>$) $z_{eq}{}^{y}$ has a correlation coefficient equal to -~-0.5455.

With As in the case of $h_{eq}{}^{y}$, we found with the use of multiple linear regression as in the case of $<z_{eq}^{pa}>$, we determined the slow (up to ~-10 m/year) and statistically insignificant linear trend in

~~$< z_{eq} >$~~of $z_{eq}{}^{y}$ as a function of latitude~~ in the range of 55ºS-55ºN (see Figure 20). One can see a tendency to decrease $< z_{eq} >$ at most latitudes with trend up to -10 m/year, but with high uncertainty. Applying~~. Moreover, the regression analysis ~~to~~of latitude-averaged ~~$< z_{eq} >$ gives us the trend equal to -4.48±6.73 m/year.~~$z_{eq}{}^{y}$ also revealed a statistically insignificant trend.

6 Discussion

The NOCE boundary is an important technical ~~characteristics~~characteristic for ~~the~~ correct application of the NOCE approximation to retrieve the nighttime distributions of minor chemical species of MLT. ~~Remind also, that Belikovich~~Kulikov et al. (2019) repeated the O and H retrieval by Mlynczak et al. (2018) ~~found by 3D simulation~~from the SABER data for the year 2004. It was revealed that the application of the NOCE condition below the boundary obtained according to the criterion could lead to a great (up to 5–8 times) systematic underestimation of O concentration below 86 km, whereas it was insignificant for H retrieval. The results presented in Figures 4, 5 and 11 demonstrate that~~ the~~, except for high northern latitudes, there is a stable annual cycle of the NOCE boundary. The monthly mean boundary can rise up to geometrical altitudes of 82-83 km (~(5.2-6.2)·10^{-3} hPa) at low latitudes and up to 84-85 km (~(3.7-4.4)·10^{-3} hPa) at middle and high latitudes. Thus, the SABER O data below these altitudes/pressures may be essentially incorrect and the retrieval approaches without using the NOCE condition (e.g., Panka et al., 2018) should be more appropriate.

Note that the NOCE condition was used not only for O and H derivation from satellite data. This assumption is a useful approach helping (i) to study hydroxyl emission in the MLT region with simulated and measured data, in particular, OH* mechanisms, morphology and variability caused, for example, by atmospheric tides and gravity wave activity (e.g., Marsh et al., 2006; Nikoukar et al., 2007; Xu et al., 2010, 2012; Kowalewski et al., 2014; Sonnemann et al., 2015); (ii) to analyze the MLT response to sudden stratospheric warmings (SSWs) (e.g., Smith et al., 2009); (iii) to derive exothermic heating rates of MLT (e.g., Mlynczak et al., 2013b); (iv) to analytically simulate the mesospheric OH* layer response to gravity waves (e.g., Swenson and Gardner, 1998); and (v) to derive the analytical dependence of excited hydroxyl layer ~~well repeats spatiotemporal variability of the NOCE boundary. Let discus the obtained results from the point of view~~number density and peak altitude on atomic oxygen and temperature (e.g., Grygalashvyly et al., 2014; Grygalashvyly, 2015). Perhaps some results require revision or reanalysis taking the NOCE boundary into account. For example, Smith et al. (2009) used the NOCE condition to analyze the ozone perturbation in the MLT, in particular, during the SSW at the beginning of 2009 (the central day was January 24). Our preliminary results of processing the SABER and simulated data in January 2009 show that the NOCE boundary above 70ºN may jump from ~80 km to ~90-95 km due to a short-time abrupt temperature fall above 80 km during this SSW. Thus, one can assume that the NOCE condition is not a good approximation for the description of ozone variations directly in the process of SSWs. This case will be studied in a separate work. Note also that after the SSW of January 2009 there began a long-time (several tens of days) event of elevated (up to ~80-85 km) stratopause (see, e.g., Figure 1 in Smith et al. (2009)), which led to the corresponding increase of temperature above 80 km. The occurrence of this event and its duration are in a good correlation with sharp lowering of the NOCE boundary at high northern latitudes (see Figures 4 and 11). Moreover, all abrupt changes of the NOCE boundary at these latitudes in January-March of other ~~possible applications of this feature.~~years (2004, 2006, 2010, 2012, 2013, 2018, and 2019) can be also associated with the elevated stratopause events in these years (see García-Comas et al. (2020) and references there).

~~The carried out analysis revealed unusual behavior of~~ According to the used chemical-transport model, the NOCE boundary ~~at the north pole latitudes in January-February 2004, 2006, 2009, 2010, 2012, 2013, 2018~~reproduces well the transition zone dividing deep and ~~2019. All these time periods are known for strong local changes of the middle atmosphere dynamics due to extremely powerful sudden stratospheric warming which leaded to appearance of elevated (from typical 50-60 km to ~80 km) stratopause events~~weak diurnal oscillations of O and H (see ~~García-Comas et al. (2020) and references there). Thus, we can speculate that~~ Figures 1-3). We verified this feature with the annual run of SD-WACCM-X model for the year 2017 provided by the NCAR High Altitude Observatory (https://doi.org/10.26024/5b58-nc53). Despite the low time resolution of the downloaded data (3-hour averaging), we obtained the results (see Figure 13) similar to Figures 1-3. Note also that both models give the same consistence between the altitudes of the NOCE boundary ~~of NOCE is sensitive to sporadic abrupt changes in the dynamics of the middle atmosphere~~and the mentioned transition zone at high latitudes in spring and autumn.

The space-time evolution of the NOCE boundary expressed in terms of ~~pseudoheights~~pressure altitudes contains a clear signal of the 11-year solar cycle in the ~~range of~~ 55ºS-55ºN range, which is suppressed mainly at high latitudes. The weak correlation of ~~z_{eq}^{pa}~~$h_{eq}{}^{y}$ with $F_{10.7}$ index at ~~south~~ high southern latitudes may be caused by the mentioned data gaps ~~due to~~specified by the satellite sensing geometry. The same reason and distortions by ~~sudden stratospheric warming,~~SSWs evidently~~,~~ determine no correlation at ~~north~~ high northern latitudes. Thus, ~~z_{eq}^{pa}~~ at low and middle latitudes $h_{eq}{}^{y}$ can be considered as a sensitive indicator of solar activity. ~~The~~Below, we present a simple and short explanation for this. Let us consider the NOCE criterion (9) at the pressure level p_{eq}:

$$VER(p_{eq}) = VER_{min}\left(T, M(p_{eq})\right).$$

In a zero approximation

$$VER_{min} = 20 \cdot \frac{k_1 \cdot O_2(p_{eq}) \cdot M(p_{eq}) \cdot \left(k_4 \cdot O_2(p_{eq}) \cdot M(p_{eq}) \cdot \left(1 - \frac{k_5 + k_6}{k_3}\right) + k_2 \cdot O_3(p_{eq})\right) \cdot A\left(T, M(p_{eq})\right)}{k_2} \cong$$

$$20 \cdot \frac{k_1 \cdot k_4 \cdot \left(O_2(p_{eq}) \cdot M(p_{eq})\right)^2 \cdot A\left(T, M(p_{eq})\right)}{k_2} \sim \frac{k_1 \cdot k_4 \cdot (p_{eq}/T)^4 \cdot A(T, p_{eq})}{k_2} \sim \frac{exp(470/T) \cdot p_{eq}{}^4 \cdot A(T, p_{eq})}{T^{8.2}},$$

where $A(T, p_{eq}) =$

$$\frac{0.47 \cdot 118.35}{215.05 + 2.5 \cdot 10^{-11} \cdot O_2/M \cdot \frac{p_{eq}}{k_B T} + 3.36 \cdot 10^{-13} \cdot e^{\frac{220}{T}} \cdot N_2/M \cdot \frac{p_{eq}}{k_B T}} + \frac{0.34 \cdot 117.21}{178.06 + 4.8 \cdot 10^{-13} \cdot O_2/M \cdot \frac{p_{eq}}{k_B T} + 7 \cdot 10^{-13} \cdot N_2/M \cdot \frac{p_{eq}}{k_B T}} +$$

$$\frac{0.47 \cdot 117.21 \cdot \left(20.05 + 4.2 \cdot 10^{-12} \cdot O_2/M \cdot \frac{p_{eq}}{k_B T} + 4 \cdot 10^{-13} \cdot N_2/M \cdot \frac{p_{eq}}{k_B T}\right)}{\left(215.05 + 2.5 \cdot 10^{-11} \cdot O_2/M \cdot \frac{p_{eq}}{k_B T} + 3.36 \cdot 10^{-13} \cdot e^{\frac{220}{T}} \cdot N_2/M \cdot \frac{p_{eq}}{k_B T}\right) \cdot \left(178.06 + 4.8 \cdot 10^{-13} \cdot O_2/M \cdot \frac{p_{eq}}{k_B T} + 7 \cdot 10^{-13} \cdot N_2/M \cdot \frac{p_{eq}}{k_B T}\right)}.$$

Our analysis of $A(T, p_{eq})$ shows that this function can be approximately rewritten as $A(T, p_{eq}) \approx const + \frac{const}{const + \frac{p_{eq}}{T}}$. So, one can see that VER_{min} is strongly dependent on T. Moreover, it anticorrelates with T. Gan et al. (2017) and Zhao et al. (2020) analyzed the simulated and measured data and revealed a clear correlation between the MLT temperature above 80 km and the 10.7-cm solar radio flux. Moreover, the dependence of the correlation coefficient of T with $F_{10.7}$ index on latitude in the 55°S-55°N range given in Figure 9 in the paper by of Zhao et al. (2020) is consistent with our Figure 9 (left panel), taking into account the sign of the correlation. Thus, we can conclude that the found anticorrelation of the NOCE boundary $h_{eq}{}^y$ with solar activity is caused by the strong connection with temperature, which, in turn, is in a good correlation with the $F_{10.7}$ index. A detailed analysis of the reasons why the solar cycle ~~does not manifest~~weakly manifests itself in the spatio-temporal variability of ~~z_{eq} requires a separate study~~ $z_{eq}{}^y$ is not so simple and is beyond the scope of this work.

~~Figures 6 and 15 present~~ Figure 5 illustrates an interesting peculiarity. At middle latitudes, the summer ~~z_{eq}~~~~pa~~$h_{eq}{}^m$ and ~~z_{eq}~~$z_{eq}{}^m$ are remarkably (~~for~~by several kilometers) higher than the winter ones, while the opposite relationship could be expected. Due to more effective daytime HO_x photoproduction at these altitudes, the summer H values at the beginning of ~~nights~~the night are higher than the ones in winter. So, the summer ozone lifetimes should be ~~less~~shorter and the NOCE condition ~~of NOCE~~ is more ~~favorable~~favourable than in winter. Nevertheless, the same ratio between the summer and winter ~~the~~ NOCE boundaries at middle latitudes was revealed in Belikovich et al. (2018) and Kulikov et al. (2018a), where the boundary of this equilibrium was determined by direct comparison of O_3 and $O_3{}^{eq}$

concentrations from results of ~~3-D~~3D chemical-transport models. Based on the results ~~in~~of Section 3, ~~one~~we can assume that the discussed effect is connected with the height position of the transition zone, which demonstrates the same variation (see Figures 1-3). Kulikov et al. (2023) derived the equations describing pure chemical O and H nighttime evolution:

$$\begin{cases} \frac{dO}{dt} = -2 \cdot k_4 \cdot M \cdot O_2 \cdot H - 2 \cdot k_2 \cdot H \cdot O_3 \\ \frac{dH}{dt} = -2 \cdot k_4 \cdot M \cdot O_2 \cdot \frac{k_5+k_6}{k_3} \cdot \frac{H^2}{O} \end{cases} .$$

(~~10~~12)

)

Neglecting the second term in the first equation as a secondary one, this system can be solved analytically ~~solved~~, so that the nighttime evolution times of O and H are~~ as follows~~:

$$\tau_O \equiv \frac{O}{|dO/dt|} = \frac{1}{2 \cdot k_4 \cdot M \cdot O_2} \cdot \left(\frac{O}{H}\right)_{t=t_{bn}} - \left(1 - \frac{k_5+k_6}{k_3}\right) \cdot (t - t_{bn}),$$

(~~11~~13)

)

$$\tau_H \equiv \frac{H}{|dH/dt|} = \frac{1}{2 \cdot k_4 \cdot M \cdot O_2} \cdot \frac{k_3}{k_5+k_6} \cdot \left(\frac{O}{H}\right)_{t=t_{bn}} - \left(\frac{k_3}{k_5+k_6} - 1\right) \cdot (t - t_{bn}),$$

(~~12~~14)

)

where t_{bn} is the time of the beginning of the night, $\left(\frac{O}{H}\right)_{t=t_{bn}}$ is the O/H ratio ~~O/H~~ at the beginning of the night. Note that k_3 is ~~essentially~~much larger than $k_5 + k_6$ (see Table 1). ~~Basing~~Based on the daytime O and H distributions in the mesopause region obtained in Kulikov et al. (2022), we calculated ~~O/H in~~ the ratio of the summer ~~and~~O/H to the winter~~.~~ O/H (see Figure 14). During the summer, ~~this ratio~~O/H at middle latitudes is remarkably less than in winter in both, northern and southern hemispheres, whereas the air concentration ~~increases~~ and the rate of reaction R4 (see Table 1) increase due to a decrease in temperature. As ~~the~~a result, the summer τ_O and τ_H are essentially ~~less~~shorter than their winter values~~ that explain~~, which explains the summer rise of the transition zone and the NOCE boundary.

Finally, let us briefly discuss other qualitative indicators of the NOCE boundary, which could be found in the SABER database. As mentioned above, Kulikov et al. (2019) showed that the nighttime O SABER profiles are correct above the NOCE boundary, whereas the H profiles hold within the whole pressure interval. Kulikov et al. (2021) demonstrated that, in the altitude range of 80-85 km, many H profiles have a sharp jump in concentration when it increases from ~ 10^7 cm^{-3} to ~ 10^8 cm^{-3}. Our analysis with the criterion (9) shows that the altitude of these jumps can be used as a rough indicator of the NOCE boundary.

7 Conclusions

The NOCE criterion is not only ~~the~~a useful technical ~~characteristics to retrieve O~~ characteristic for the retrieval of O from satellite data, but it also reproduces the transition zone position~~,~~ which ~~divides~~separates deep and weak diurnal oscillations of O and H at low and middle latitudes.

~~The~~ At middle latitudes, the summer boundary of NOCE is remarkably (by several kilometers) higher than the winter one, which is accompanied with the same variation of the transition zone. This effect is explained by the markedly lower values of the O and H nighttime evolution times in summer than in winter by virtue of the lower values of the O/H ratio at the beginning of the night and air concentration increase.

The NOCE boundary according to the criterion is sensitive to sporadic abrupt changes in the dynamics of the middle atmosphere.

The NOCE boundary at low and middle latitudes expressed in ~~pseudoheight~~pressure altitudes contains a clear signal of 11-year solar cycle and can be considered as a sensitive indicator of solar activity.

~~At middle latitudes, summer boundary of NOCE is remarkably (for several kilometers) higher than winter one that is accompanied by the same variation of the transition zone. This effect is explained by the markedly lower values of the O and H nighttime evolution times in summer than in winter due to lower values of the ratio O/H at the beginning of the night and air concentration increase.~~

Data availability. The SABER data are obtained from the website (https://saber.gats-inc.com). The data of solar radio flux at 10.7 cm in 2002-2021 were downloaded from http://www.wdcb.ru/stp/solar/solar_flux.ru.html and https://www.spaceweather.gc.ca/forecast-prevision/solar-solaire/solarflux/sx-5-en.php.

Code availability. Code is available upon request.

Author contributions. MK and MB ~~carried out the~~performed data processing and analysis and wrote the manuscript. AC, SD, and AM contributed to reviewing the article.

Competing interests. The authors declare that they have no conflict of interest.

Acknowledgements. The authors are grateful to the SABER team for data availability.

Financial support. ~~This work was supported~~The main results presented in Section 5 were obtained under the support by the Russian Science Foundation under grant No. 22-12-00064 (https://rscf.ru/project/22-12-00064~~/) and~~/). The analysis of the difference between the NOCE boundary in summer and winter at middle latitudes and the reasons of well anticorrelation of the NOCE boundary with $F_{10.7}$ index were carried out at the expense of state assignment no. 0729-2020-0037.

References

Allen, M., Lunine, J. I., and Yung, Y. L~~.~~.: The vertical distribution of ozone in the mesosphere and lower thermosphere, J. Geophys. Res., 89(D3), 4841–4872, https://doi.org/10.1029/JD089iD03p04841, 1984.

Belikovich, M. V., Kulikov, M. Yu, Grygalashvyly, M., Sonnemann, G. R., Ermakova, T. S., Nechaev, A. A., and Feigin, A .M.: Ozone chemical equilibrium in the extended mesopause under the nighttime conditions, Adv. Space Res., 61, 426–432, https://doi.org/10.1016/j.asr.2017.10.010, 2018.

Burkholder, J. B., Sander, S. P., Abbatt, J., Barker, J. R., Cappa, C., Crounse, J. D., Dibble, T. S., Huie, R. E., Kolb, C. E., Kurylo, M. J., Orkin, V. L., Percival, C. J., Wilmouth, D. M., and Wine, P. H.: Chemical Kinetics and Photochemical Data for Use in Atmospheric Studies, Evaluation No. 19, JPL Publication 19-5, Jet Propulsion Laboratory, Pasadena, http://jpldataeval.jpl.nasa.gov, 2020.

Evans, W. F. J., McDade, I. C., Yuen, J., and Llewellyn, E. J.: A rocket measurement of the O_2 infrared atmospheric (0-0) band emission in the dayglow and a determination of the mesospheric ozone and atomic oxygen densities, Can. J. Phys., 66, 941–946, https://doi.org/10.1139/p88-151. 1988.

Gan, Q., Du, J., Fomichev, V. I., Ward, W. E., Beagley, S. R., Zhang, S., and Yue, J.: Temperature responses to the 11 year solar cycle in the mesosphere from the 31 year (1979–2010) extended Canadian Middle Atmosphere Model simulations and a comparison with the 14 year (2002–2015) TIMED/SABER observations, J. Geophys. Res. Space Physics, 122, 4801–4818, https://doi.org/10.1002/2016JA023564, 2017.

García-Comas, M., Funke, B., López-Puertas, M., González-Galindo, F., Kiefer, M., and Höpfner, M.: First detection of a brief mesoscale elevated stratopause in very early winter. Geophys. Res. Lett., 47, e2019GL086751, https://doi.org/10.1029/2019GL086751, 2020.

Good, R. E.: Determination of atomic oxygen density from rocket borne measurements of hydroxyl airglow, Planet. Space Sci., 24, 389–395, https://doi.org/10.1016/0032-0633(76)90052-0, 1976.

Grygalashvyly, M., Sonnemann, G. R., and Hartogh, P.: Long-term behavior of the concentration of the minor constituents in the mesosphere - A model study, Atmos. Chem. Phys., 9, 2779–2792, https://doi.org/10.5194/acp-9-2779-2009, 2009.

Grygalashvyly, M., Sonnemann, G. R., Lübken, F.-J., Hartogh, P., and Berger, U.: Hydroxyl layer: Mean state and trends at midlatitudes, J. Geophys. Res. Atmos., 119, 12,391–12,419, https://doi.org/10.1002/2014JD022094, 2014.

Grygalashvyly, M.: Several notes on the OH* layer, Ann. Geophys., 33, 923-930, https://doi.org/10.5194/angeo-33-923-2015, 2015.

Hartogh, P., Jarchow, C., Sonnemann, G. R., and Grygalashvyly, M.: On the spatiotemporal behavior of ozone within the upper mesosphere/mesopause region under nearly polar night conditions, J. Geophys. Res., 109, D18303, https://doi.org/10.1029/2004JD004576, 2004.

Hartogh, P., Jarchow, Ch., Sonnemann, G. R., and Grygalashvyly, M.: Ozone distribution in the middle latitude mesosphere as derived from microwave measurements at Lindau (51.66°N, 10.13°E), J. Geophys. Res., 116, D04305, https://doi.org/10.1029/2010JD014393, 2011.

Feigin, A. M., Konovalov, I. B., and Molkov, Y. I.: Towards understanding nonlinear nature of atmospheric photochemistry: Essential dynamic model of the mesospheric photochemical system., J. Geophys. Res.: Atmos., 103, 25,447–25,460, https://doi.org/10.1029/98JD01569, 1998.

Konovalov, I. B., and Feigin, A. M.: Towards an understanding of the non-linear nature of atmospheric photochemistry: origin of the complicated dynamic behavior of the mesospheric photochemical system, Nonlin. Processes Geophys., 87-104, https://doi.org/10.5194/npg-7-87-2000, 2000.

Körner, U., and Sonnemann, G. R.: Global 3D-modeling of water vapor concentration of the mesosphere/mesopause region and implications with respect to the NLC region, J. Geophys. Res., 106, 9639– 9651, https://doi.org/10.1029/2000JD900744, 2001.

Kowalewski, S., v. Savigny, C., Palm, M., McDade, I. C., and Notholt, J.: On the impact of the temporal variability of the collisional quenching process on the mesospheric OH emission layer: a study based on SD-WACCM4 and SABER, Atmos. Chem. Phys., 14, 10193-10210, https://doi.org/10.5194/acp-14-10193-2014, 2014.

Kremp, C., Berger, U., Hoffmann, P., Keuer, D., and Sonnemann, G. R.: Seasonal variation of middle latitude wind fields of the mesopause region—A comparison between observation and model calculation, Geophys. Res. Lett., 26, 1279–1282, https://doi.org/10.1029/1999GL900218, 1999.

Kulikov, M. Yu., and Feigin, A. M.: Reactive-diffusion waves in the mesospheric photochemical system. Adv. Space Res., 35(11), 1992-1998, https://doi.org/10.1016/j.asr.2005.04.020, 2005.

Kulikov, M. Yu.: Theoretical investigation of the influence of a quasi 2-day wave on nonlinear photochemical oscillations in the mesopause region, J. Geophys. Res., 112, D02305, https://doi.org/10.1029/2005JD006845, 2007.

Kulikov, M. Y., Belikovich, M. V., Grygalashvyly, M., Sonnemann, G. R., Ermakova, T. S., Nechaev, A. A., and Feigin, A. M.: Daytime ozone loss term in the mesopause region, Ann. Geophys., 35, 677-682 https://doi.org/10.5194/angeo-35-677-2017, 2017.

Kulikov, M. Y., Belikovich, M. V., Grygalashvyly, M., Sonnemann, G. R., Ermakova, T. S., Nechaev, A. A., and Feigin, A. M.: Nighttime ozone chemical equilibrium in the mesopause region. J. Geophys. Res.,123, 3228–3242, https://doi.org/10.1002/2017JD026717, 2018a.

Kulikov, M. Y., Nechaev, A. A., Belikovich, M. V., Ermakova, T. S., and Feigin, A. M.: Technical note: Evaluation of the simultaneous measurements of mesospheric OH, HO_2, and O_3 under a photochemical equilibrium assumption – a statistical approach, Atm. Chem. Phys., 18, 7453-747, https://doi.org/10.5194/acp-18-7453-2018, 2018b.

Kulikov, M. Yu., Nechaev, A. A., Belikovich, M. V., Vorobeva, E. V., Grygalashvyly, M., Sonnemann, G. R., and Feigin, A. M.: Border of nighttime ozone chemical equilibrium in the mesopause region from saber data: implications for derivation of atomic oxygen and atomic hydrogen, Geophys. Res. Lett., 46, 997– 1004, https://doi.org/10.1029/2018GL080364, 2019.

Kulikov, M. Y., Belikovich, M. V., and Feigin, A. M.: Analytical investigation of the reaction-diffusion waves in the mesopause photochemistry, J. Geophys. Res., 125, e2020JD033480, https://doi.org/10.1029/2020JD033480, 2020.

Kulikov, M. Y., Belikovich, M. V., Feigin, A. M.: The 2-day photochemical oscillations in the mesopause region: the first experimental evidence? Geophys. Res. Lett., 48, e2021GL092795, https://doi.org/10.1029/2021GL092795, 2021.

Kulikov, M. Y., Belikovich, M. V., Grygalashvyly, M., Sonnemann, G. R., and Feigin, A.M.: The revised method for retrieving daytime distributions of atomic oxygen and odd-hydrogens in the mesopause region from satellite observations, Earth Planets Space, 74, 44, https://doi.org/10.1186/s40623-022-01603-8, 2022.

Kulikov, M. Yu., Belikovich, M. V., Chubarov, A. G., Dementeyva, S. O., Feigin, A. M.: Boundary of nighttime ozone chemical equilibrium in the mesopause region: improved criterion of determining the boundary from satellite data, Adv. Space Res., 71 (6), 2770-2780, https://doi.org/10.1016/j.asr.2022.11.005, 2023.

Llewellyn, E. J., McDade, I. C. Moorhouse, P. and Lockerbie M. D.: Possible reference models for atomic oxygen in the terrestrial atmosphere, Adv. Space Res., 13, 135–144, https://doi.org/10.1016/0273-1177(93)90013-2, 1993.

Llewellyn, E. J., and McDade, I. C.: A reference model for atomic oxygen in the terrestrial atmosphere, Adv. Space Res., 18, 209–226, https://doi.org/10.1016/0273-1177(96)00059-2, 1996.

Lübken, F.-J., Berger, U. and Baumgarten, G.: Temperature trends in the midlatitude summer mesosphere, J. Geophys. Res. Atmos., 118, 13347–13360, https://doi.org/10.1002/2013JD020576, 2013.

Manney, G. L., Kruger, K., Sabutis, J. L., Sena, S. A., and Pawson, S.: The remarkable 2003–2004 winter and other recent warm winters in the Arctic stratosphere since the late 1990s. J. Geophys. Res., 110, D04107, https://doi.org/10.1029/2004JD005367, 2005.

Marsh, D. R., Smith, A. K., Mlynczak, M. G., and Russell III, J. M.: SABER observations of the OH Meinel airglow variability near the mesopause, J. Geophys. Res., 111, A10S05, https://doi.org/10.1029/2005JA011451, 2006.

McDade, I. C., Llewellyn, E. J., and Harris, F. R.: Atomic oxygen concentrations in the lower auroral thermosphere, Adv. Space Res., 5, 229–232, https://doi.org/10.1029/GL011I003P00247, 1985.

McDade, I. C., and Llewellyn, E. J.: Mesospheric oxygen atom densities inferred from night-time OH Meinel band emission rates, Planet. Space Sci., 36, 897–905, https://doi.org/10.1016/0032-0633(88)90097-9, 1988.

Mlynczak, M. G., Marshall, B. T., Martin-Torres, F. J., Russell III, J. M., Thompson, R. E., Remsberg, E. E., and Gordley, L. L.: Sounding of the Atmosphere using Broadband Emission Radiometry observations of daytime mesospheric $O_2(^1D)$ 1.27 µm emission and derivation of ozone, atomic oxygen, and solar and chemical energy deposition rates, J. Geophys. Res., 112, D15306, https://doi.org/10.1029/2006JD008355, 2007.

Mlynczak, M. G., Hunt, L. A., Mast, J. C., Marshall, B. T., Russell III, J. M., Smith, A. K., Siskind, D. E., Yee, J.-H., Mertens, C. J., Martin-Torres, F. J., Thompson, R. E., Drob, D. P., and Gordley, L. L.: Atomic oxygen in the mesosphere and lower thermosphere derived from SABER: Algorithm theoretical basis and measurement uncertainty, J. Geophys. Res., 118, 5724–5735, https://doi.org/10.1002/jgrd.50401, 2013a.

Mlynczak, M. G., Hunt, L. H., Mertens, C. J., Marshall, B. T., Russell III, J. M., López-Puertas, M., Smith, A. K., Siskind, D. E., Mast, J. C., Thompson, R. E., and Gordley, L. L.: Radiative and energetic constraints on the global annual mean atomic oxygen concentration in the mesopause region, J. Geophys. Res. Atmos., 118, 5796–5802, https://doi.org/10.1002/jgrd.50400, 2013b.

Mlynczak, M. G., Hunt, L. A. Marshall, B. T. Mertens, C. J. Marsh, D. R. Smith, A. K. Russell, J. M. Siskind D. E., and Gordley L. L.: Atomic hydrogen in the mesopause region derived from SABER: Algorithm theoretical basis, measurement uncertainty, and results, J. Geophys. Res., 119, 3516–3526, https://doi.org/10.1002/2013JD021263, 2014.

Mlynczak, M. G., Hunt, L. A., Russell, J. M. III, and Marshall, B. T.: Updated SABER night atomic oxygen and implications for SABER ozone and atomic hydrogen, Geophys. Res. Lett., 45, 5735–5741, https://doi.org/10.1029/2018GL077377, 2018.

Morton, K. W., and Mayers, D. F.; Numerical Solution of Partial Differential Equations, Cambridge University Press, 1994.

Nikoukar, R., Swenson, G. R., Liu, A. Z., and Kamalabadi, F.: On the variability of mesospheric OH emission profiles, J. Geophys. Res., 112, D19109, https://doi.org/10.1029/2007JD008601, 2007.

Panka, P. A., Kutepov, A. A., Rezac, L., Kalogerakis, K. S., Feofilov, A. G., Marsh, D., Janches, D., and Yiğit, E. Atomic oxygen retrieved from the SABER 2.0- and 1.6- μm radiances using new first-principles nighttime OH(v) model, Geophys. Res. Lett., 45, 5798–5803, https://doi.org/10.1029/2018GL077677, 2018.

Pendleton, W. R., Baker, K. D., Howlett, L. C.: Rocket-based investigations of O(^{3}P), O_2 ($a^1\Delta_g$) and OH* (v=1,2) during the solar eclipse of 26 February 1979, J. Atm. Terr. Phys., 45(7), 479-491, 1983.

Siskind, D. E., Marsh, D. R., Mlynczak, M. G., Martin-Torres, F. J., and Russell III, J. M.: Decreases in atomic hydrogen over the summer pole: Evidence for dehydration from polar mesospheric clouds? Geophys. Res. Lett., 35, L13809, https://doi.org/10.1029/2008GL033742, 2008.

Siskind, D. E., Mlynczak, M. G., Marshall, T., Friedrich, M., Gumbel, J.: Implications of odd oxygen observations by the TIMED/SABER instrument for lower D region ionospheric modeling, J. Atmos. Sol. Terr. Phys., 124, 63–70, https://doi.org/10.1016/j.jastp.2015.01.014, 2015.

Schmidlin, F .J.: First observation of mesopause temperature lower than 100 K, Geophys. Res. Lett., 19, 1643-1646, https://doi.org/10.1029/92GL01506, 1992.

Shimazaki, T.: Minor Constituents in the Middle Atmosphere, D. Reidel, Norwell, Mass., USA, 444 pp., 1985.

Smith, A. K., Lopez-Puertas, M., Garcıa-Comas, M. and Tukiainen, S.: SABER observations of mesospheric ozone during NH late winter 2002–2009, Geophys. Res. Lett., 36, L23804, https://doi.org/10.1029/2009GL040942, 2009.

Smith, A. K., Marsh, D. R. Mlynczak, M. G. and Mast, J. C.: Temporal variations of atomic oxygen in the upper mesosphere from SABER, J. Geophys. Res., 115, D18309, https://doi.org/10.1029/2009JD013434, 2010.

Sonnemann, G., and Fichtelmann, B.: Enforced oscillations and resonances due to internal non-linear processes of photochemical system in the atmosphere, Acta. Geod. Geophys. Mont. Hung., 22, 301–311, 1987.

Sonnemann, G., and Fichtelmann, B.: Subharmonics, cascades of period of doubling and chaotic behavior of photochemistry of the mesopause region, J. Geophys. Res., 101, 1193-1203, https://doi.org/10.1029/96JD02740, 1997.

Sonnemann, G., Kremp, C. Ebel, A. and Berger U.: A three-dimensional dynamic model of minor constituents of the mesosphere, Atmos. Environ., 32, 3157–3172, https://doi.org/10.1016/S1352-2310(98)00113-7, 1998.

Sonnemann, G., Feigin, A. M., and Molkov, Ya. I.: On the influence of diffusion upon the nonlinear behaviour of the photochemistry of the mesopause region, J. Geophys. Res., 104, 30591-30603, https://doi.org/10.1029/1999JD900785, 1999.

Sonnemann, G., and Feigin, A. M.: Non-linear behaviour of a reaction-diffusion system of the photochemistry within the mesopause region, Phys. Rev. E, 59, 1719-1726, https://doi.org/10.1103/PhysRevE.59.1719, 1999.

Sonnemann, G. R.: The photochemical effects of dynamically induced variations in solar insolation, J. Atmos. Sol. Terr. Phys., 63, 781-797, https://doi.org/10.1016/S1364-6826(01)00010-4, 2001.

Sonnemann, G. R., and Grygalashvyly, M.: On the two-day oscillations and the day-to-day variability in global 3-D-modeling of the chemical system of the upper mesosphere/mesopause region, Nonlin. Processes Geophys., 12, 691– 705, https://doi.org/10.5194/npg-12-691-2005, 2005.

Sonnemann, G. R., Hartogh, P., Berger, U., and Grygalashvyly, M.: Hydroxyl layer: trend of number density and intra-annual variability, Ann. Geophys., 33, 749–767, https://doi.org/10.5194/angeo-33-749-2015, 2015.

Swenson, G. R., and Gardner C. S.: Analytical models for the responses of the mesospheric OH* and Na layers to atmospheric gravity waves, J. Geophys. Res., 103(D6), 6271–6294, https://doi.org/10.1029/97JD02985, 1998.

Thomas, G. E., Olivero, J. J., Jensen, E. J., Schroder, W., and Toon, O. B.: Relation between increasing methane and the presence of ice clouds at the mesopause, Nature, 338, 490–492https://doi.org/10.1038/338490a0, 1989.

Thomas, R. J.: Atomic hydrogen and atomic oxygen density in the mesosphere region: Global and seasonal variations deduced from Solar Mesosphere Explorer near-infrared emissions, J. Geophys. Res., 95, 16,457–16,476, https://doi. org/ 10. 1029/ JD095 iD10p 16457, 1990.

Thomas, G. E.: Mesospheric clouds and the physics of the mesopause region, Rev. Geophys., 29, 553–575, https://doi.org/10.1029/91RG01604, 1991.

Walcek, C. J.: Minor flux adjustment near mixing ratio extremes for simplified yet highly accurate monotonic calculation of tracer advection, J. Geophys. Res., 105, 9335-9348, https://doi.org/10.1029/1999JD901142, 2000.

Xu, J., Smith, A. K., Jiang, G., Gao, H., Wei, Y., Mlynczak, M. G., and Russell III, J. M.: Strong longitudinal variations in the OH nightglow, Geophys. Res. Lett., 37, L21801, https://doi.org/10.1029/2010GL043972, 2010.

Xu, J., Gao, H. Smith, A. K. and Zhu Y.: Using TIMED/SABER nightglow observations to investigate hydroxyl emission mechanisms in the mesopause region, J. Geophys. Res., 117, D02301, https://doi.org/10.1029/2011JD016342, 2012.

Zhao, X. R., Sheng, Z. Shi, H. Q. Weng, L. B. and He Y.: Middle Atmosphere Temperature Changes Derived from SABER Observations during 2002–20, J. Climate, 34, 7995–8012, https://doi.org/10.1175/JCLI-D-20-1010.1, 2021.

Table 1. List of reactions with corresponding reaction rates (for three-body reactions [cm^6 $molecule^{-2}$ s^{-1}], for two-body reactions [cm^3 $molecule^{-1}$ s^{-1}]) taken from Burkholder et al. (2020).

	Reaction	Rate constant
R1	$O+O_2+M \rightarrow O_3+M$	$k_1 = 6.1 \cdot 10^{-34}(298/T)^{2.4}$
R2	$H+O_3 \rightarrow O_2+OH$	$k_2 = 1.4 \cdot 10^{-10} exp(-470/T)$
R3	$O+HO_2 \rightarrow O_2+OH$	$k_3 = 3 \cdot 10^{-11} exp(200/T)$
R4	$H+O_2+ M \rightarrow HO_2+M$	$k_4 = 5.3 \cdot 10^{-32}(298/T)^{1.8}$
R5	$H+HO_2 \rightarrow O_2+H_2$	$k_5 = 6.9 \cdot 10^{-12}$
R6	$H+HO_2 \rightarrow O+H_2O$	$k_6 = 1.6 \cdot 10^{-12}$

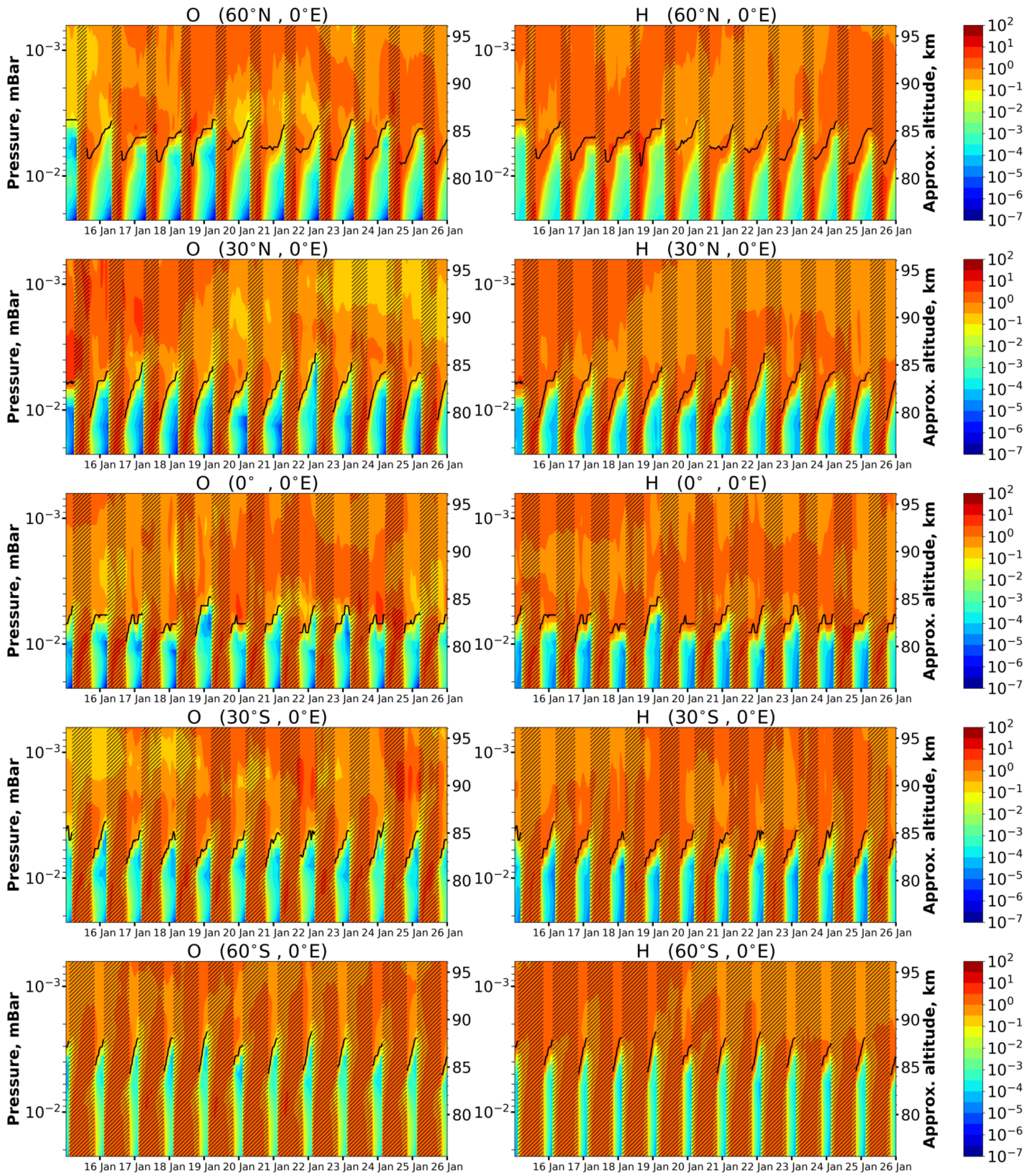

Figure 1. O and H time-height variations above different points in January 2000 calculated by ~~the~~ 3D chemical transport model of ~~the~~ middle atmosphere. ~~The concentrations~~ Concentrations are normalized by mean daily values, correspondingly ~~The dark~~, calculated as a function of altitude. Dark bars mark daytime, light bars mark nighttime. ~~The magenta~~Black lines point the NOCE boundary altitude in accordance to criterion (5) (Cr = 0.1).

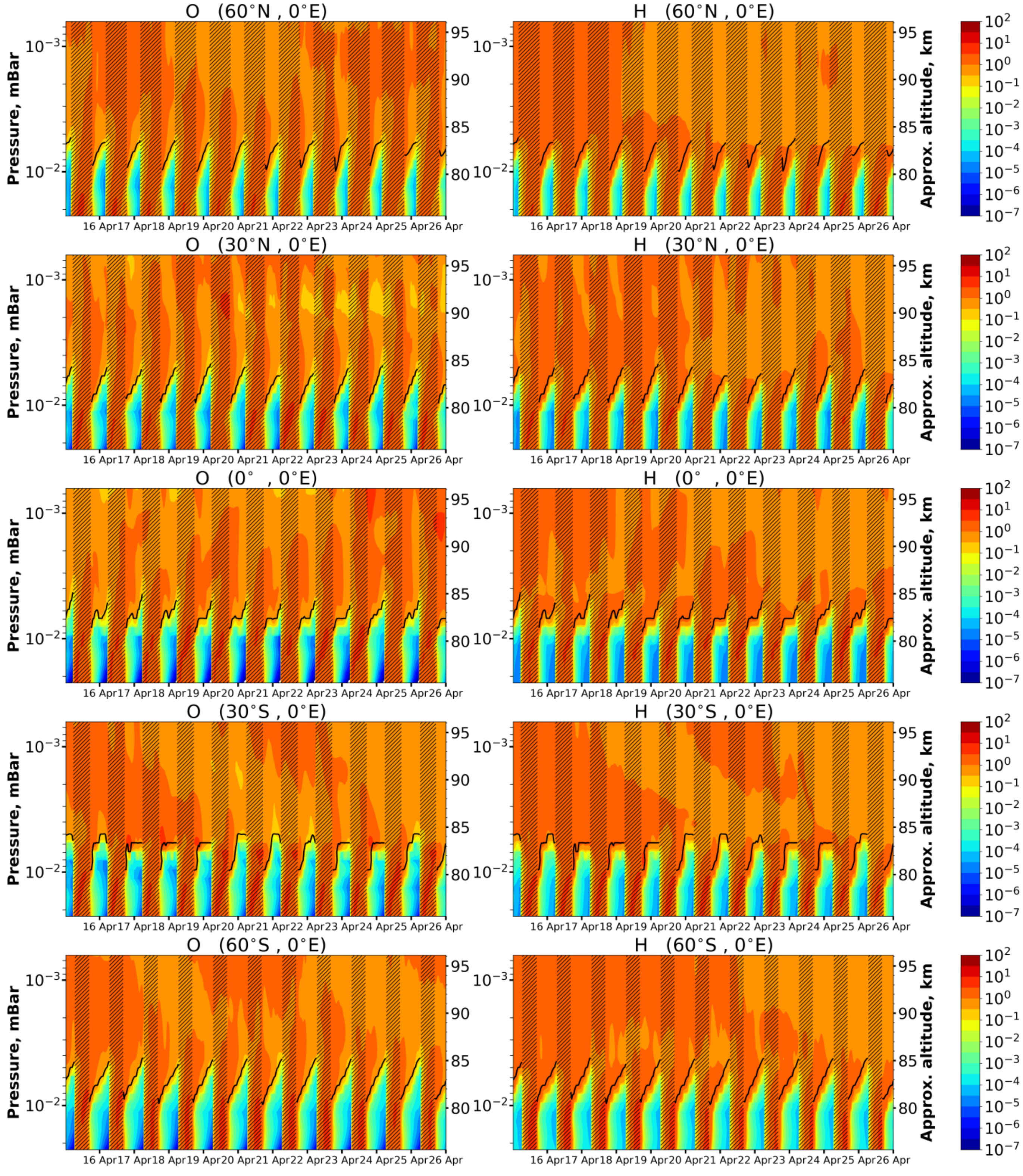

Figure 2. The same as in Fig. 1, but in April~~.~~ 2000. Black lines point NOCE boundary altitude according to criterion (5) (Cr = 0.1).

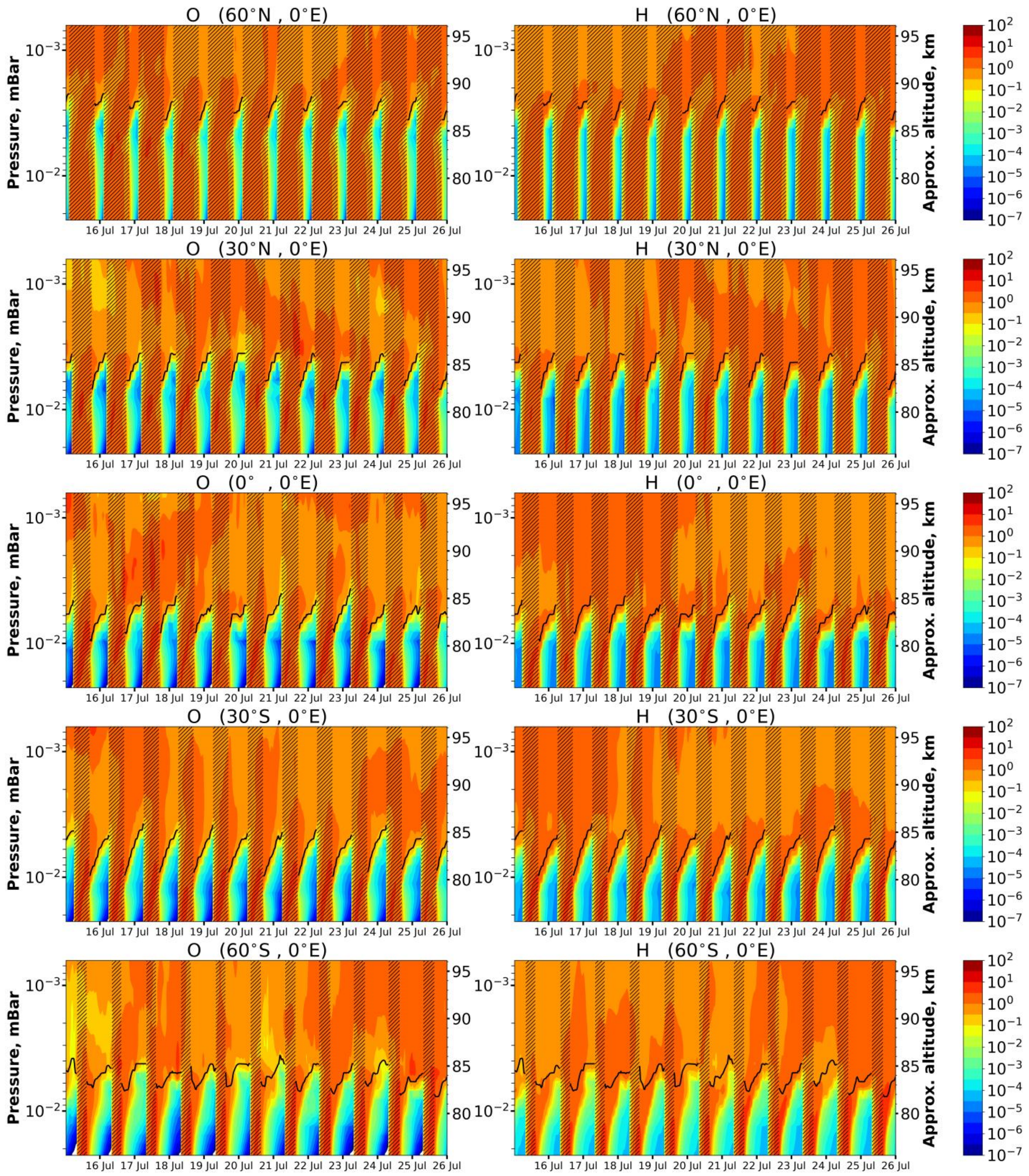

Figure 3. The same as in Fig. 1, but in July. 2000. Black lines point the NOCE boundary altitude according to criterion (5) (Cr = 0.1).

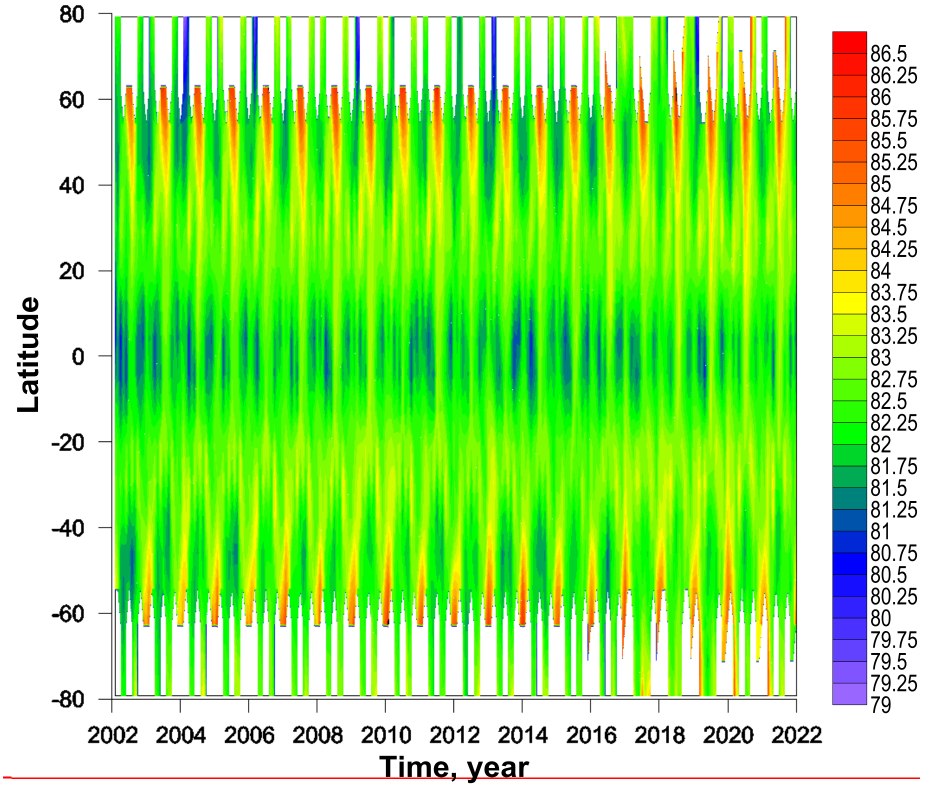
Latitude
Time, year

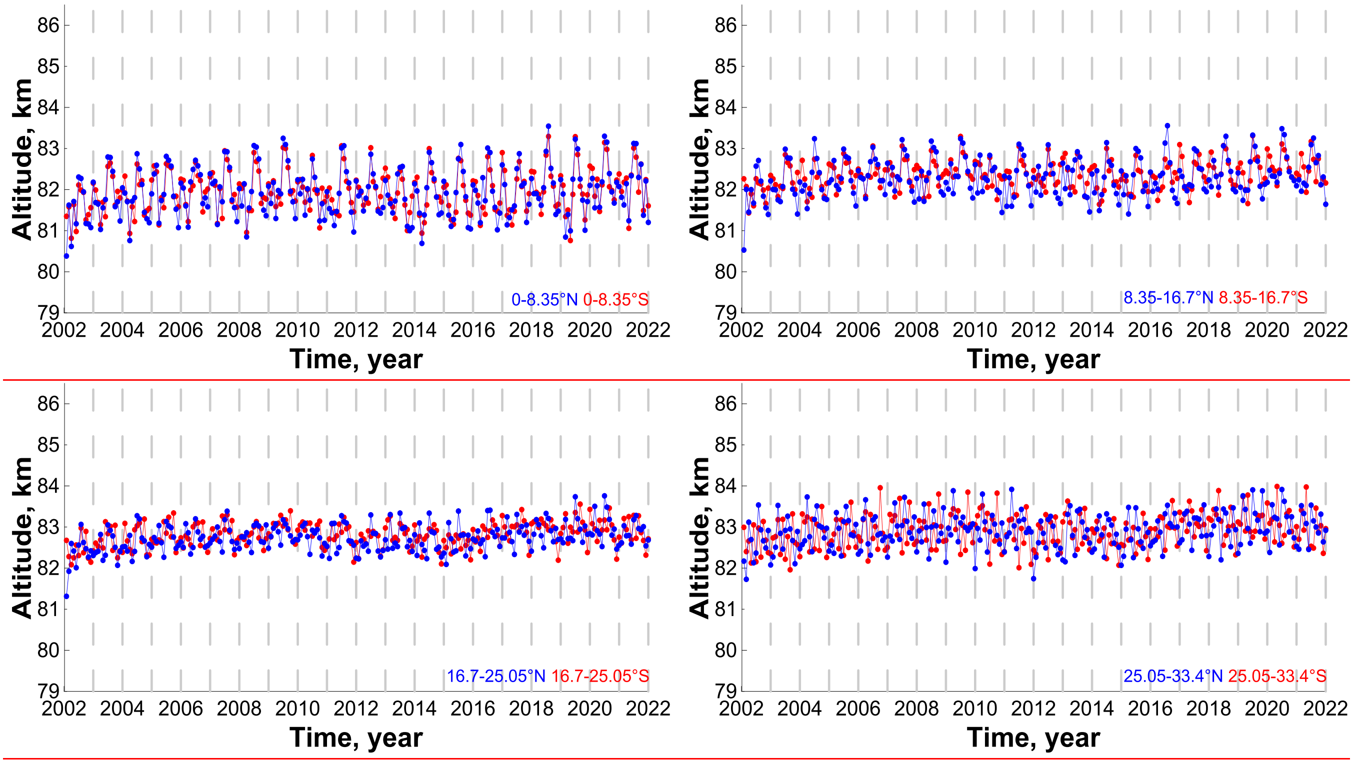
Altitude, km
Time, year
0-8.35°N 0-8.35°S
8.35-16.7°N 8.35-16.7°S
16.7-25.05°N 16.7-25.05°S
25.05-33.4°N 25.05-33.4°S

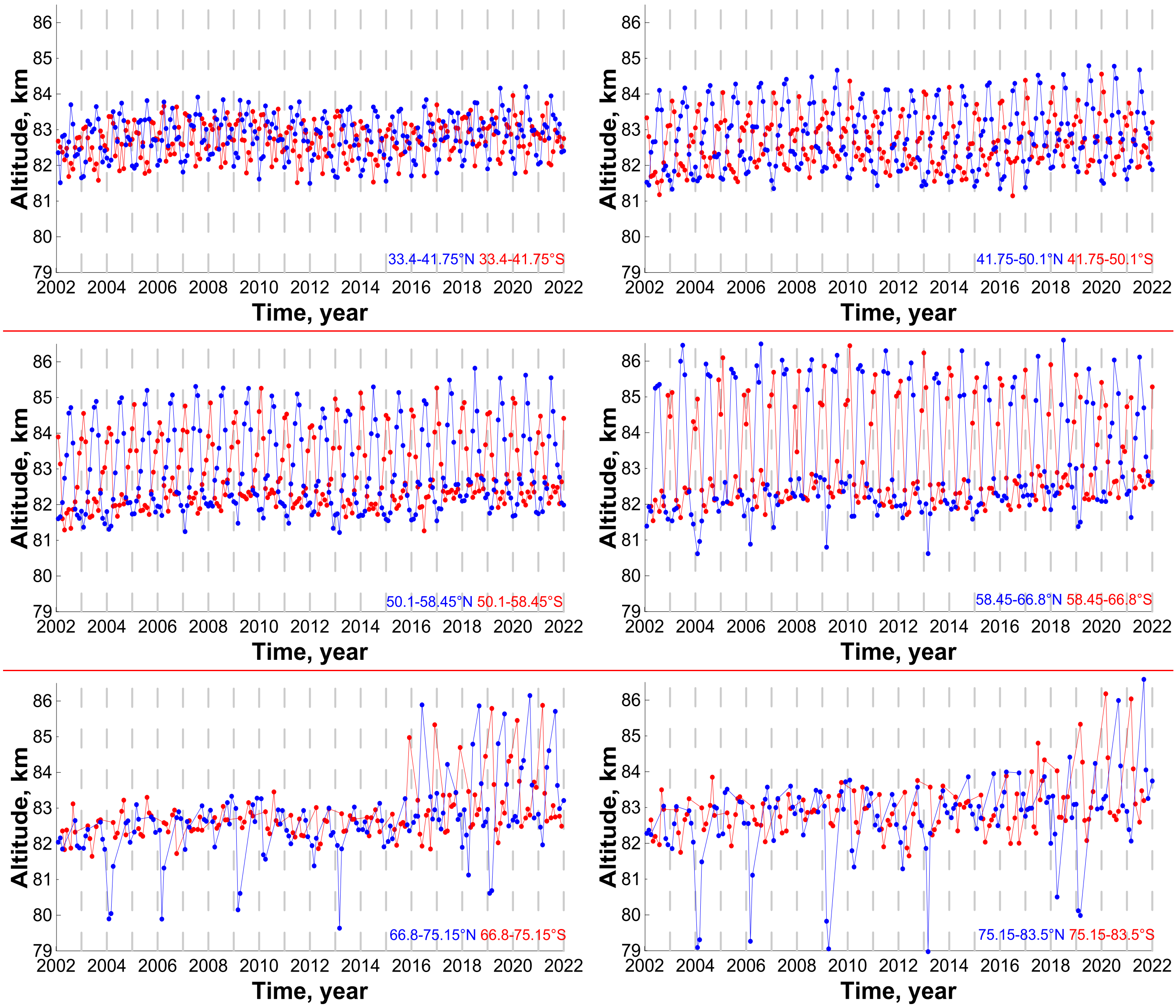

Figure 4. ~~The space-time evolution of z_{eq}^{pa}. White color indicates data gaps due to the satellite sensing geometry.~~

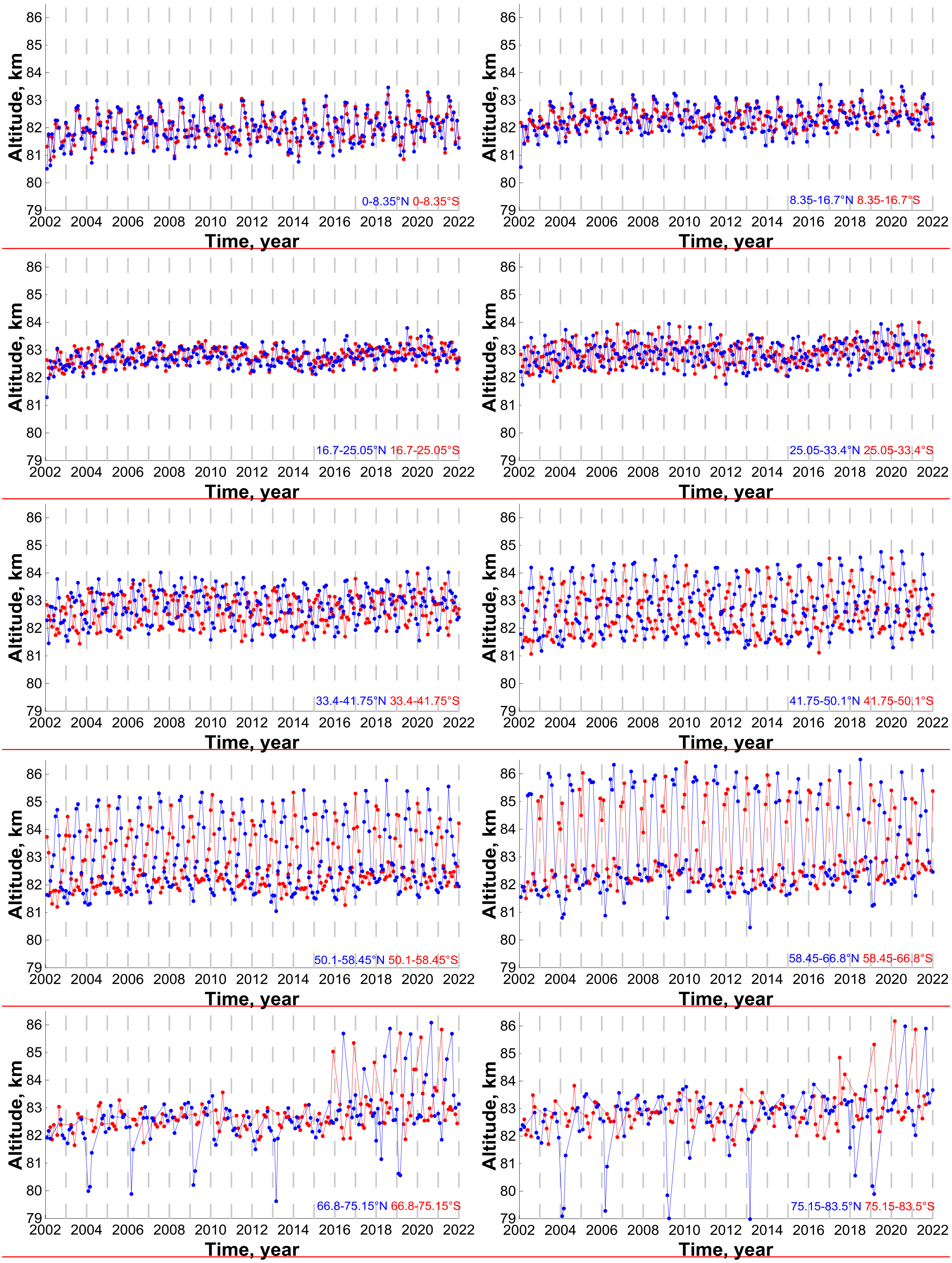

~~Figure 5. The time evolution of z_{eq}^{pa}~~Time evolution of monthly mean pressure altitude $h_{eq}{}^{m}$ at different latitudes.

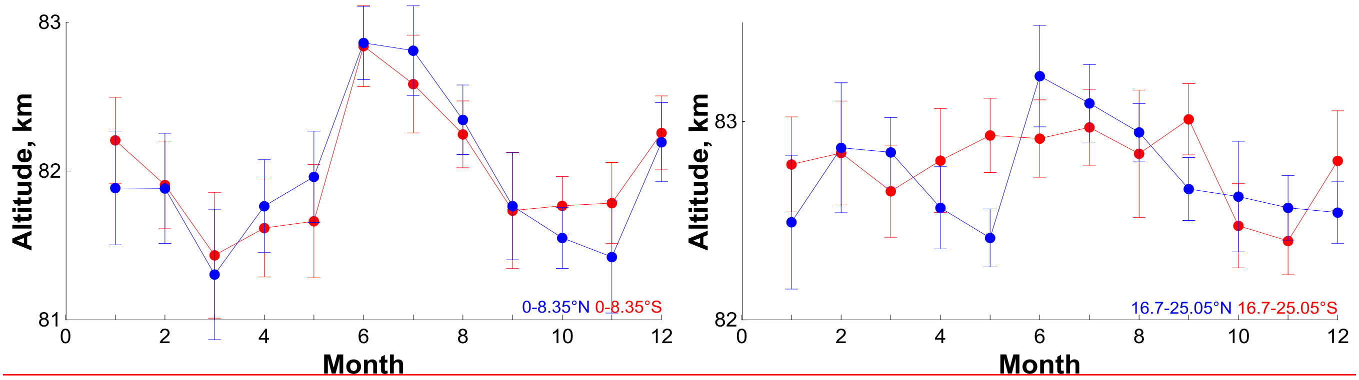
Altitude, km
Month
0-8.35°N 0-8.35°S
16.7-25.05°N 16.7-25.05°S

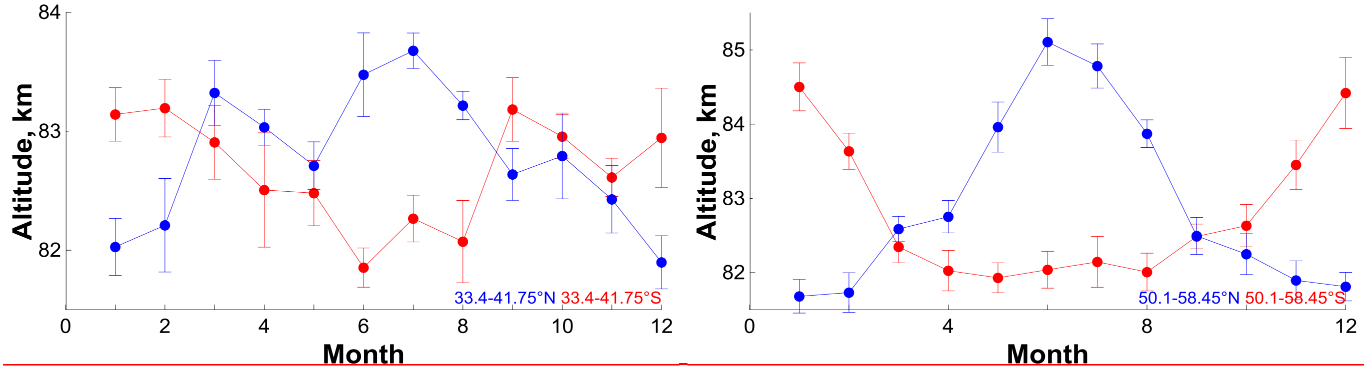
Altitude, km
Month
33.4-41.75°N 33.4-41.75°S
50.1-58.45°N 50.1-58.45°S

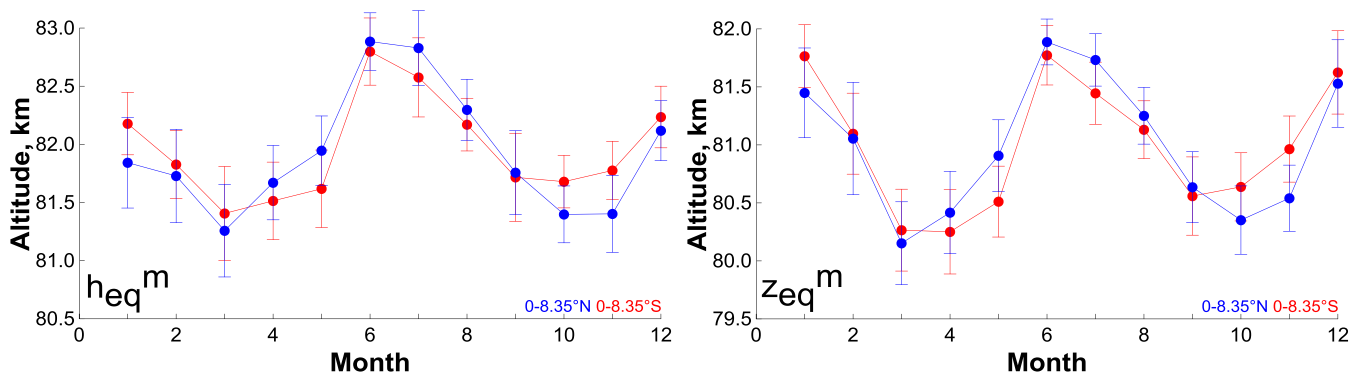
Altitude, km
Month
h_{eq}^m
z_{eq}^m
0-8.35°N 0-8.35°S

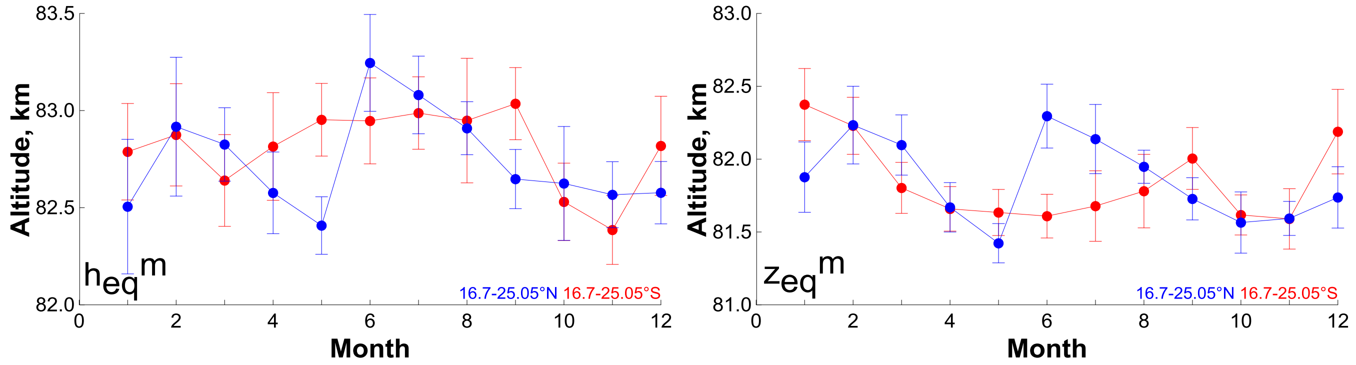
Altitude, km
Month
h_{eq}^m
z_{eq}^m
16.7-25.05°N 16.7-25.05°S

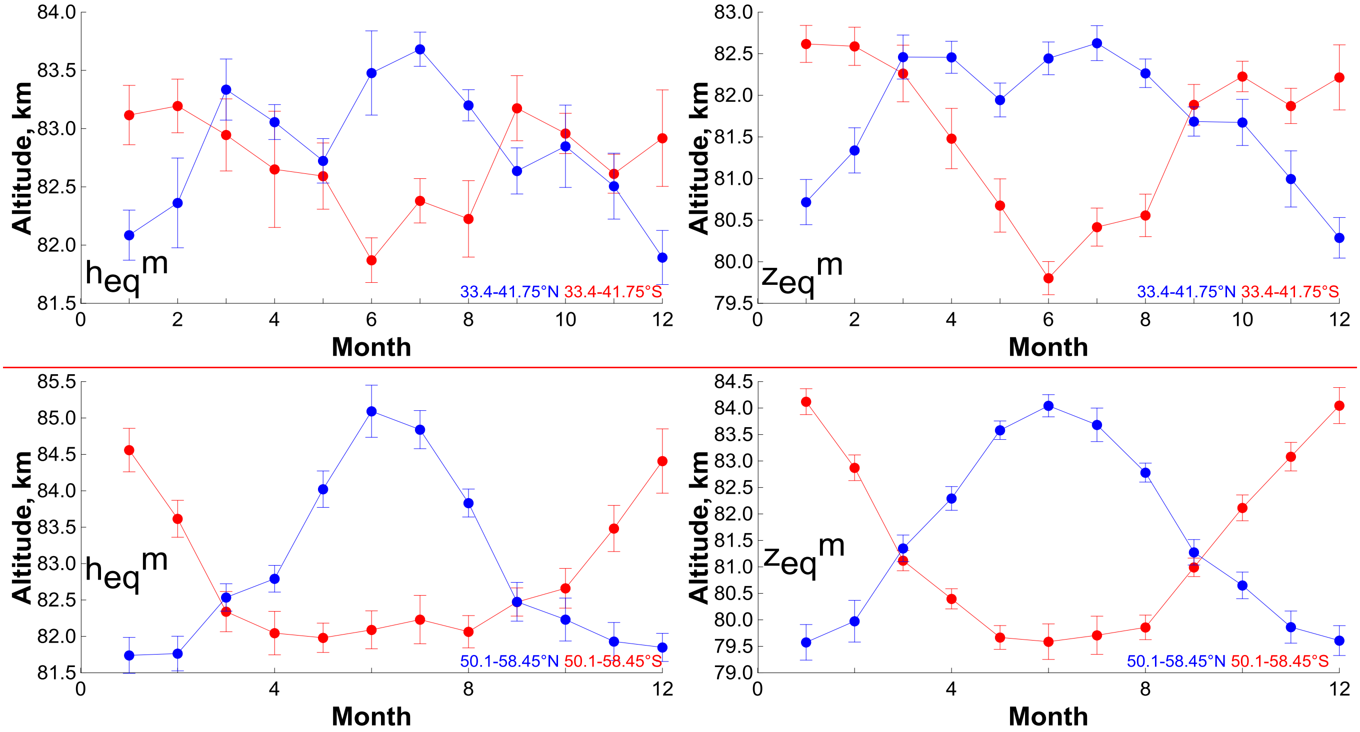

Figure 5. Figure 6. Average (for 2002-2021) annual cycle of z_{eq}^{pa} monthly mean pressure altitude h_{eq}^m and geometrical altitude z_{eq}^m at somefour specific latitudes.

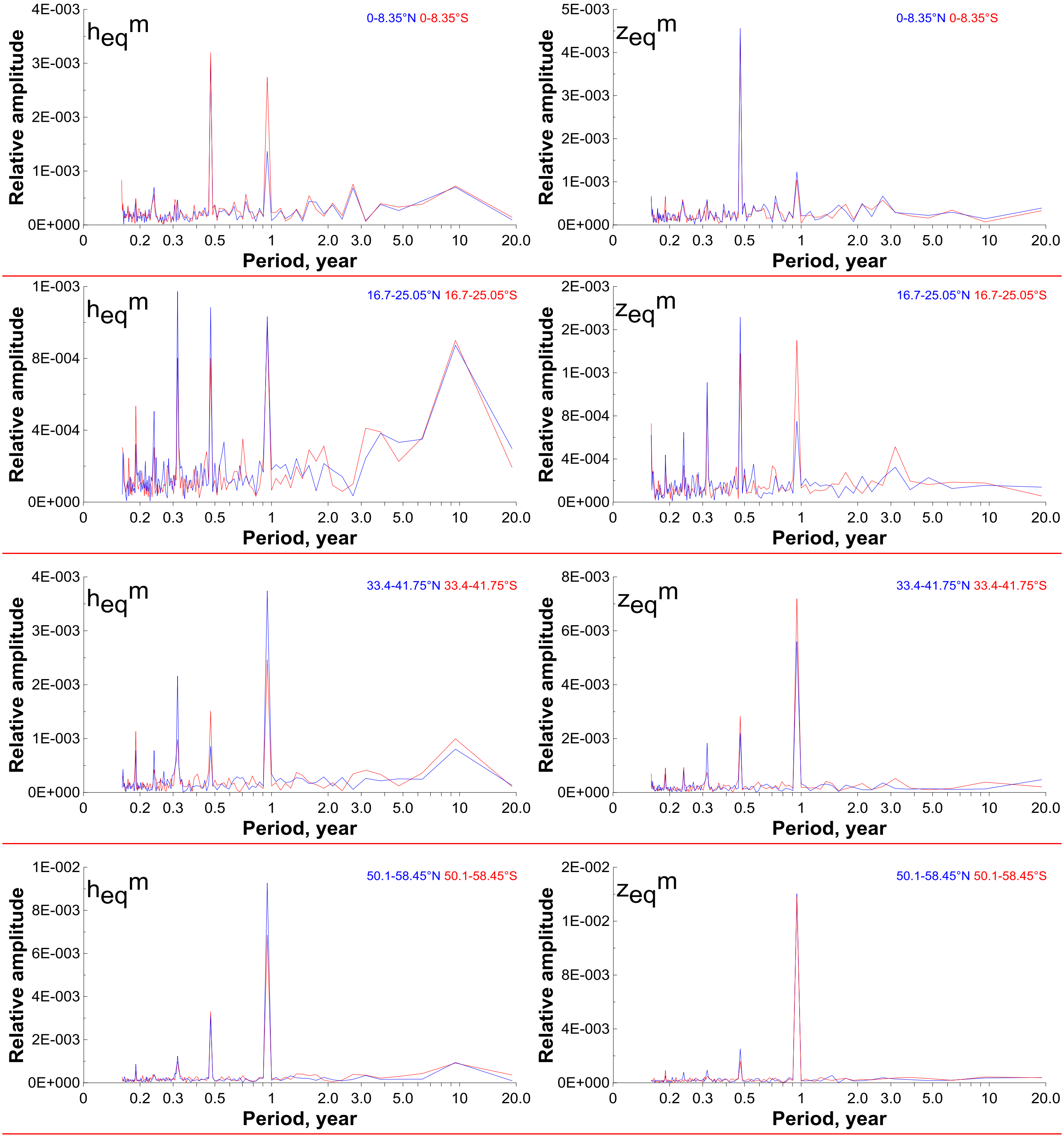
heq m
zeq m
Relative amplitude
Period, year
0 0.2 0.3 0.5 1 2.0 3.0 5.0 10 20.0
0-8.35°N 0-8.35°S
16.7-25.05°N 16.7-25.05°S
33.4-41.75°N 33.4-41.75°S
50.1-58.45°N 50.1-58.45°S
0E+000 1E-003 2E-003 3E-003 4E-003
0E+000 1E-003 2E-003 3E-003 4E-003 5E-003
0E+000 4E-004 8E-004 1E-003
0E+000 4E-004 8E-004 1E-003 2E-003 2E-003
0E+000 2E-003 4E-003 6E-003 8E-003
0E+000 2E-003 4E-003 6E-003 8E-003 1E-002
0E+000 4E-003 8E-003 1E-002 2E-002

Figure 6.

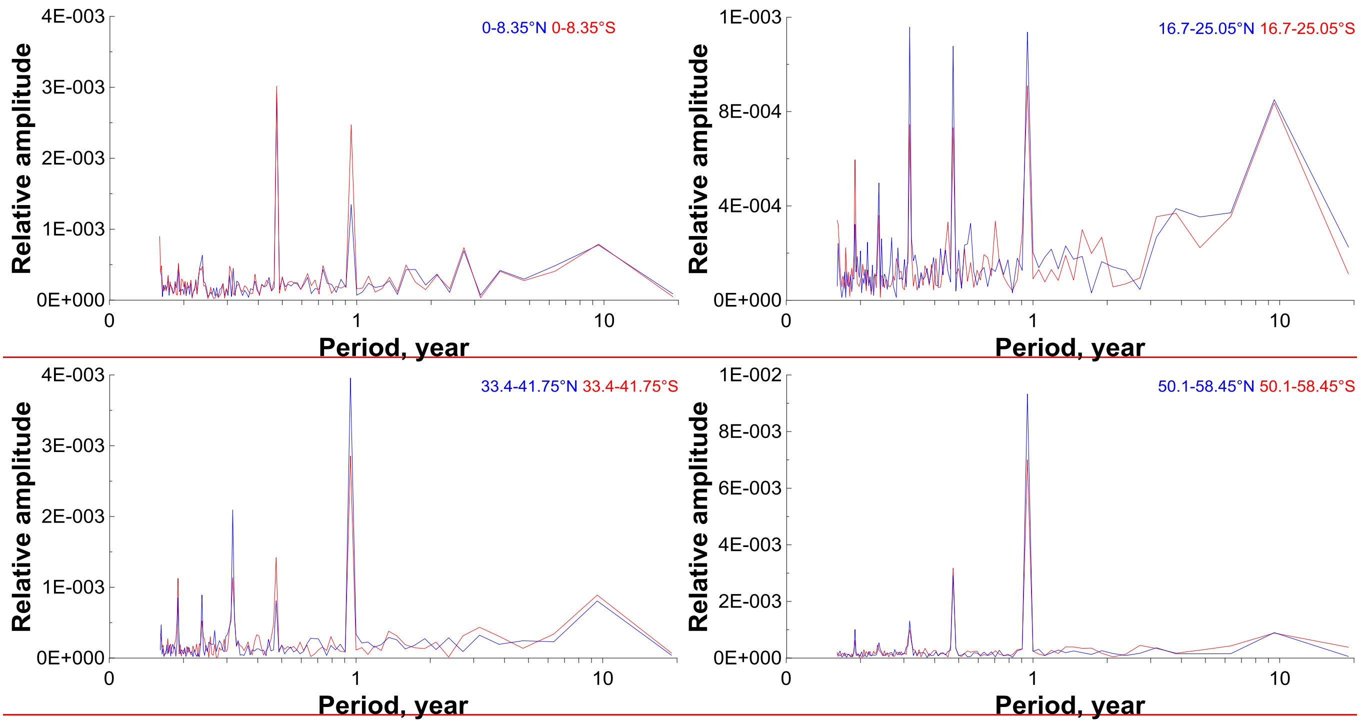

~~Figure 7.~~ ~~Fourier'~~Fourier spectra of ~~z_{eq}^{pa} time evolution~~monthly mean pressure altitude $h_{eq}{}^{m}$ and geometrical altitude $z_{eq}{}^{m}$ at ~~the same~~four specific latitudes~~ as in Figure 6.~~. In each spectrum, the amplitudes of harmonics were normalized to the corresponding zero harmonic.

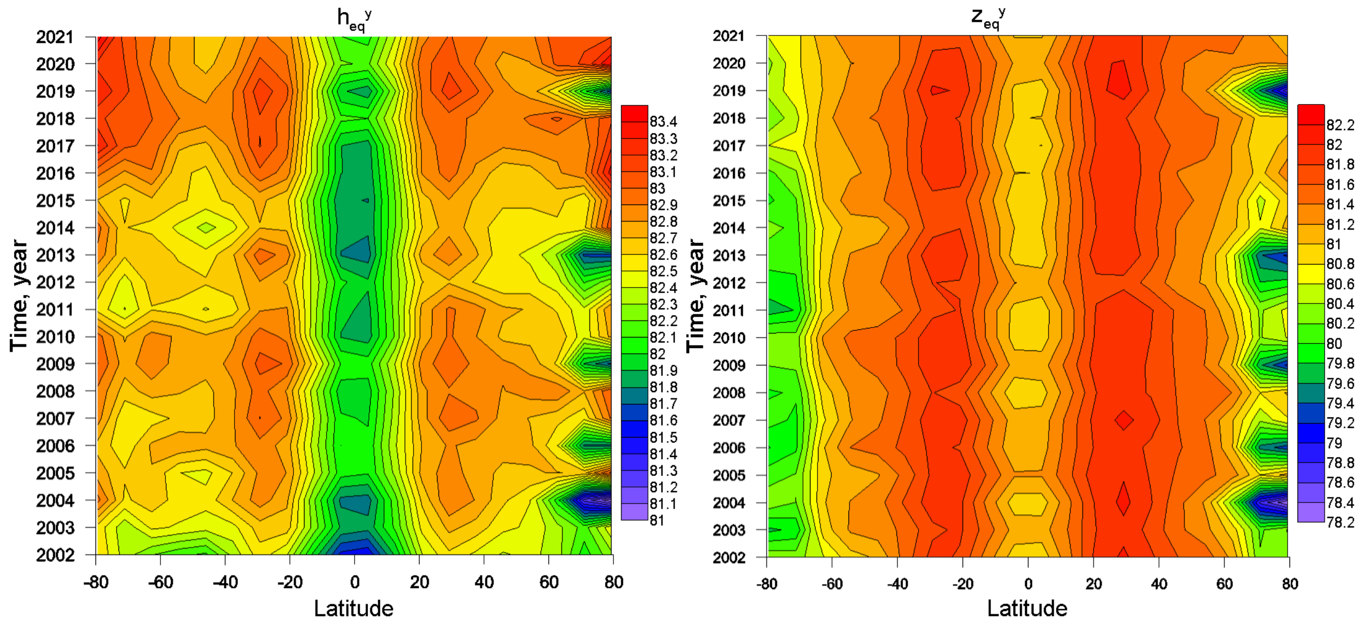

Figure 7.

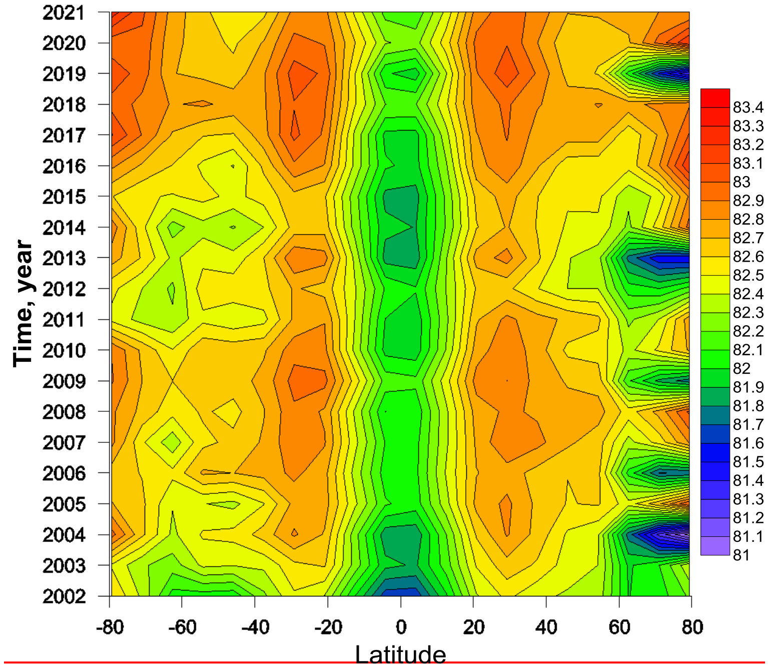

Latitude-time evolution of annually mean pressure altitude $h_{eq}{}^{y}$ (left) and geometrical altitude $z_{eq}{}^{y}$ (right).

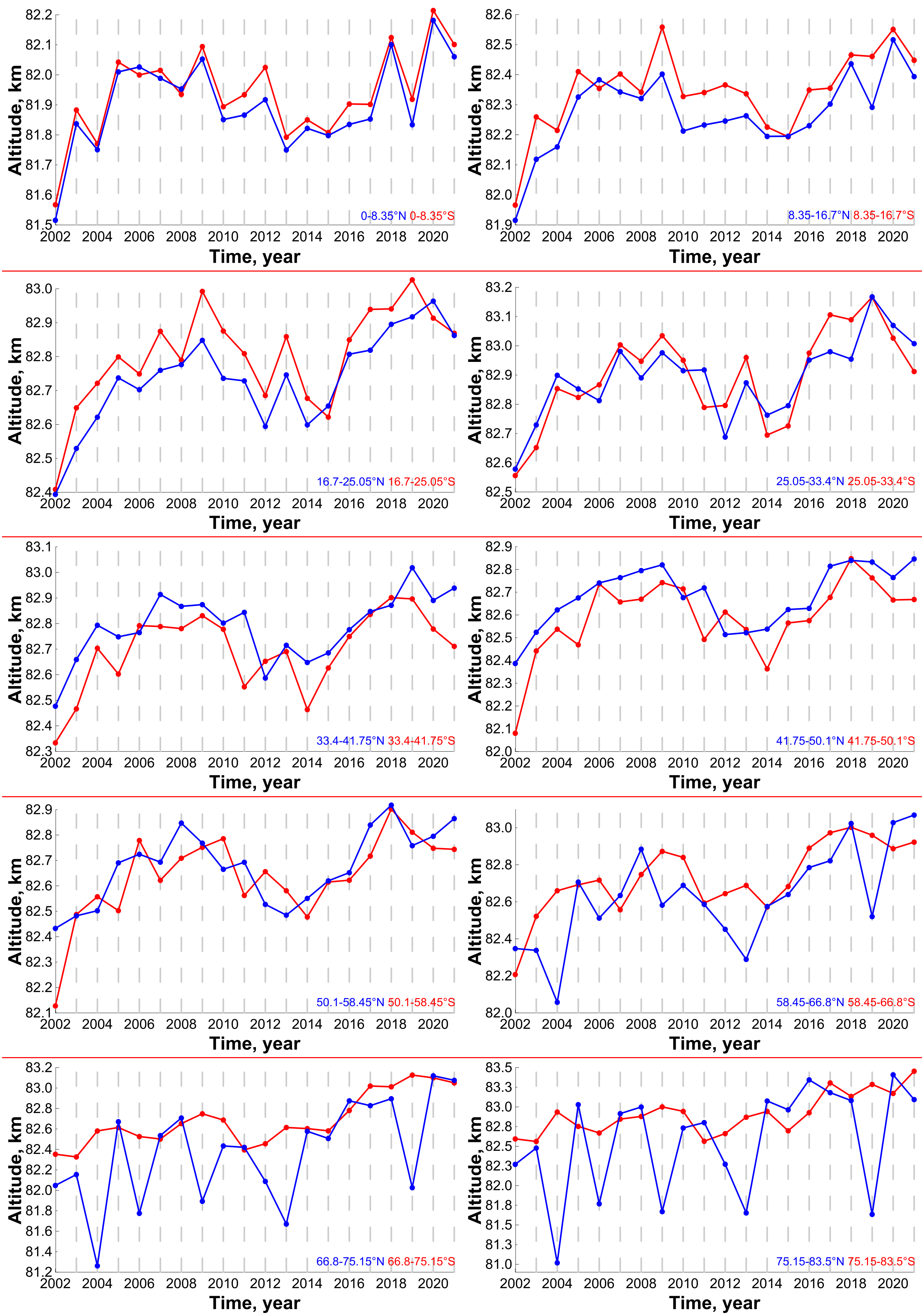
Altitude, km
Time, year
0-8.35°N 0-8.35°S
8.35-16.7°N 8.35-16.7°S
16.7-25.05°N 16.7-25.05°S
25.05-33.4°N 25.05-33.4°S
33.4-41.75°N 33.4-41.75°S
41.75-50.1°N 41.75-50.1°S
50.1-58.45°N 50.1-58.45°S
58.45-66.8°N 58.45-66.8°S
66.8-75.15°N 66.8-75.15°S
75.15-83.5°N 75.15-83.5°S

Figure 8. ~~The latitude-time~~Time evolution of ~~average annual z_{eq}^{pa}.~~

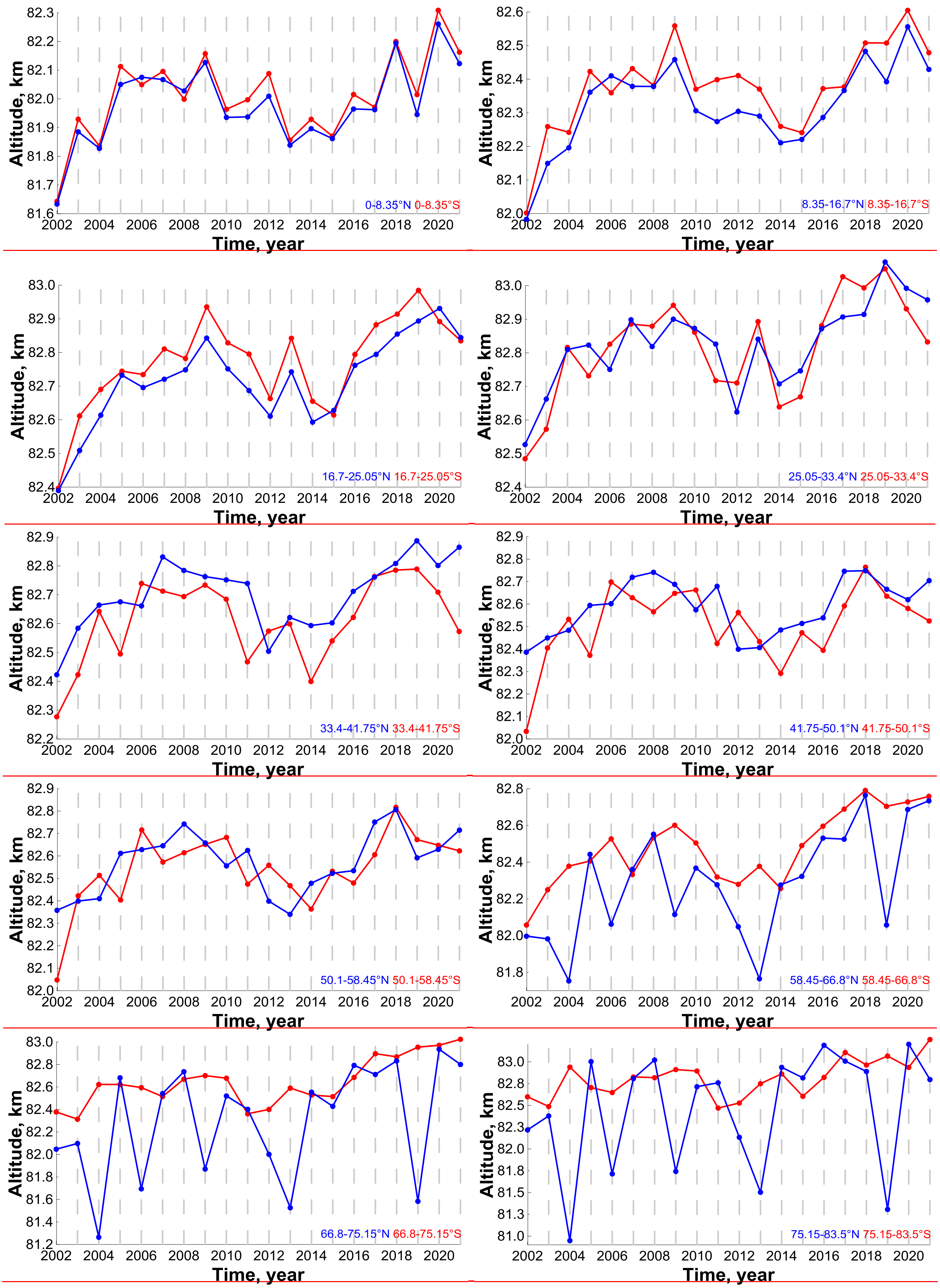
Altitude, km
Time, year
0-8.35°N 0-8.35°S
8.35-16.7°N 8.35-16.7°S
16.7-25.05°N 16.7-25.05°S
25.05-33.4°N 25.05-33.4°S
33.4-41.75°N 33.4-41.75°S
41.75-50.1°N 41.75-50.1°S
50.1-58.45°N 50.1-58.45°S
58.45-66.8°N 58.45-66.8°S
66.8-75.15°N 66.8-75.15°S
75.15-83.5°N 75.15-83.5°S

Figure 9. The time evolution of average annual z_{eq}^{pa} ($< z_{eq}^{pa} >$)annually mean pressure altitude h_{eq}^{y} at different latitudes.

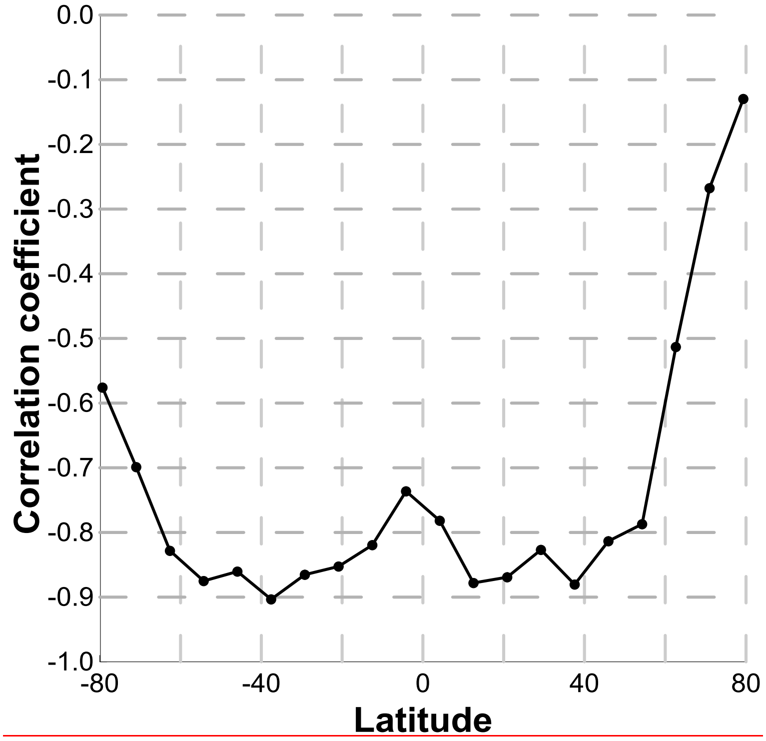

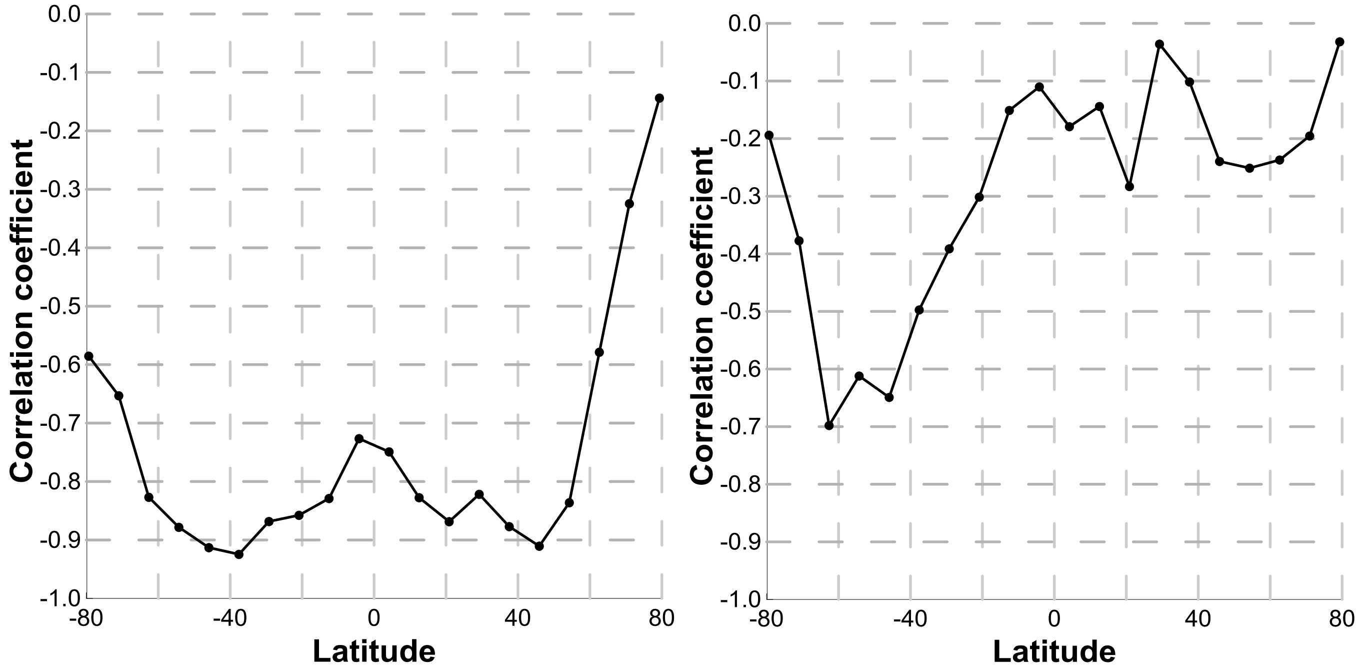

Figure 10. The correlation'9. Correlation coefficient of $< z_{eq}^{pa} >$ with $F_{10.7}$ index at different latitudeswith pressure altitude h_{eq}^{y} (left) and geometrical altitude z_{eq}^{y} (right) as a function of latitude.

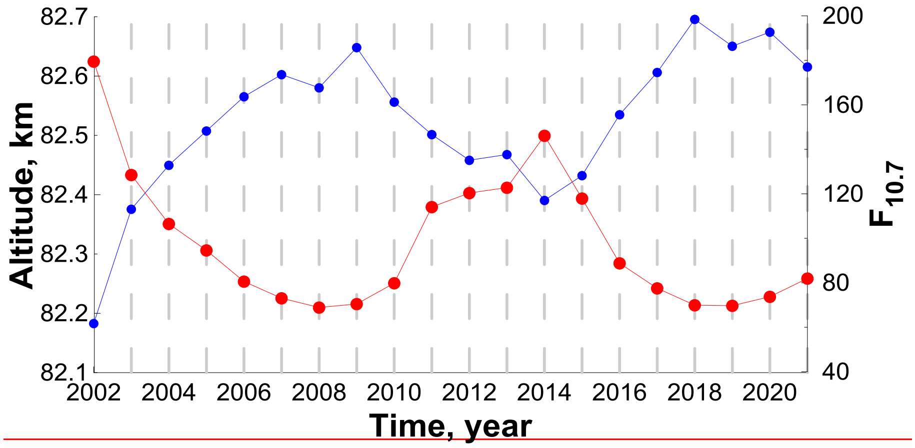

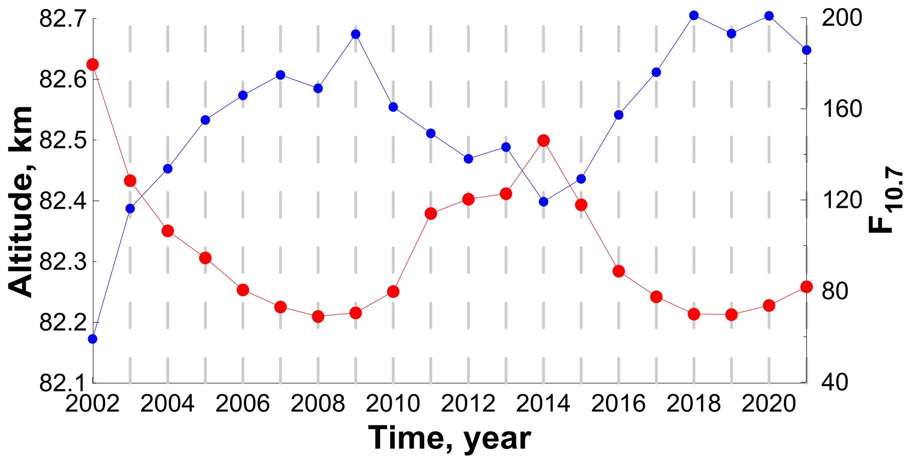

Figure 11.

Figure 10. Red curve: $F_{10.7}$ index (solar radio flux at 10.7 cm). Blue curve: latitude-averaged <zeqpa>pressure altitude *heqy* in thisthe range between ~55ºS and ~55ºN.

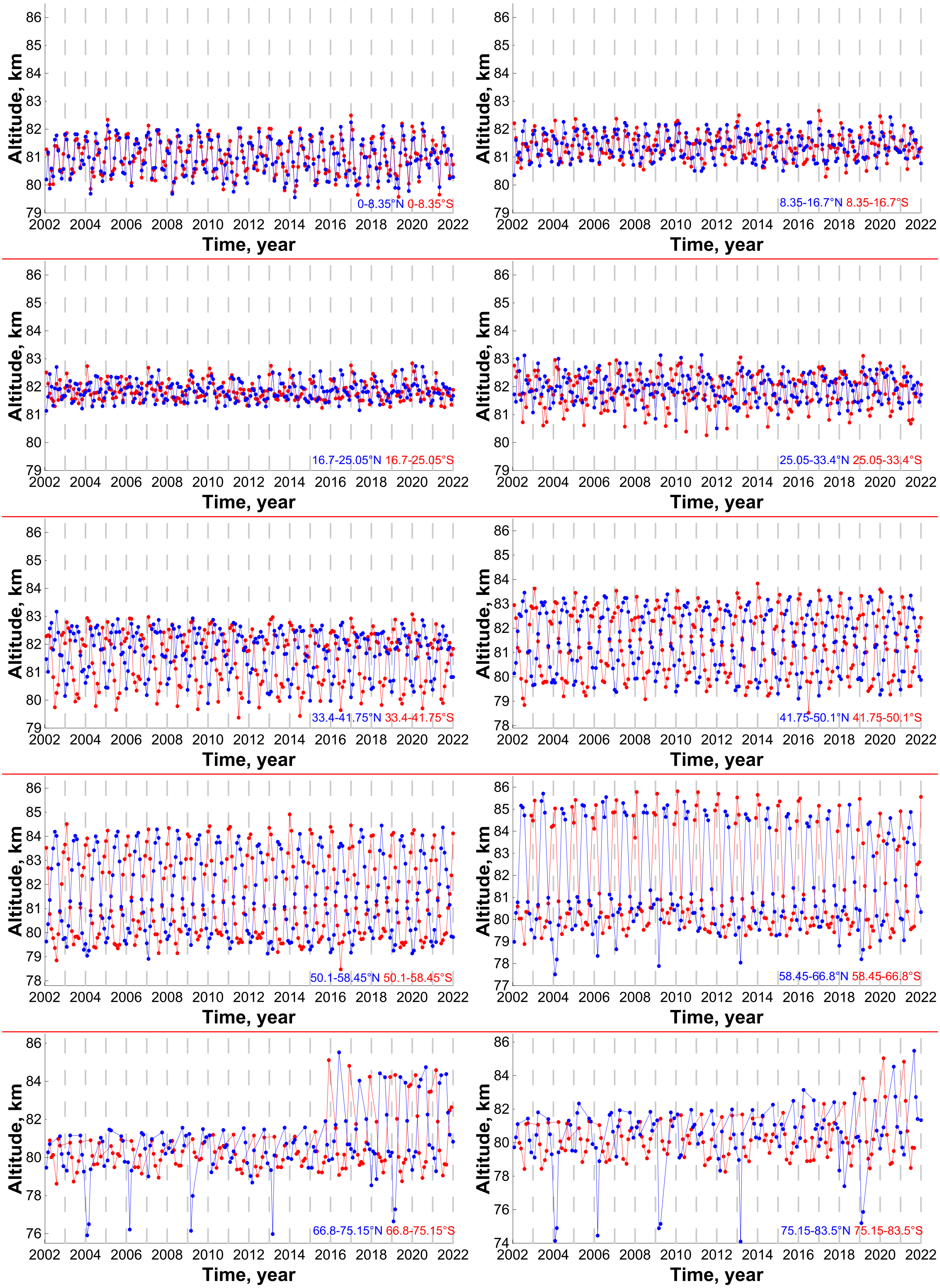

Altitude, km
Time, year
0-8.35°N 0-8.35°S
8.35-16.7°N 8.35-16.7°S
16.7-25.05°N 16.7-25.05°S
25.05-33.4°N 25.05-33.4°S
33.4-41.75°N 33.4-41.75°S
41.75-50.1°N 41.75-50.1°S
50.1-58.45°N 50.1-58.45°S
58.45-66.8°N 58.45-66.8°S
66.8-75.15°N 66.8-75.15°S
75.15-83.5°N 75.15-83.5°S

Figure 11.

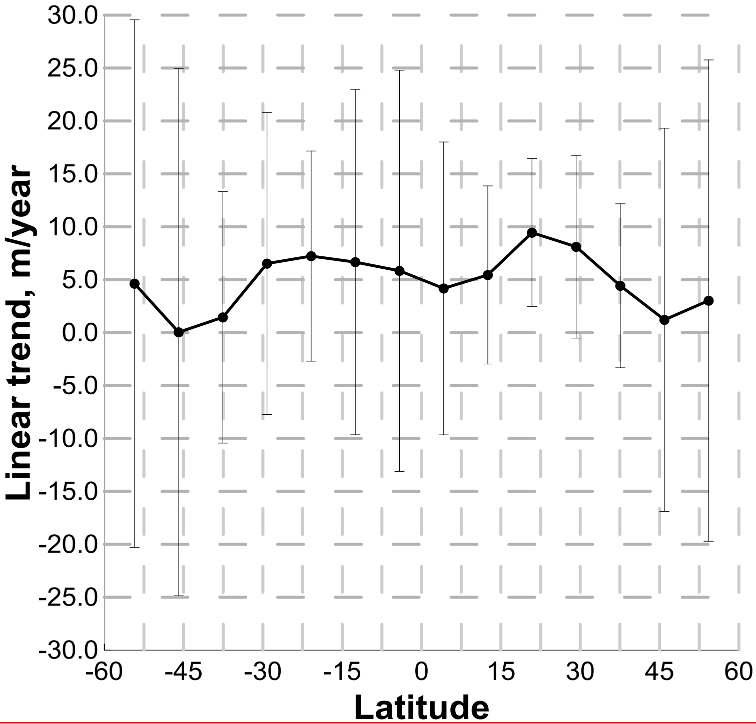

Time evolution of monthly mean geometrical altitude $z_{eq}{}^{m}$ at different latitudes.

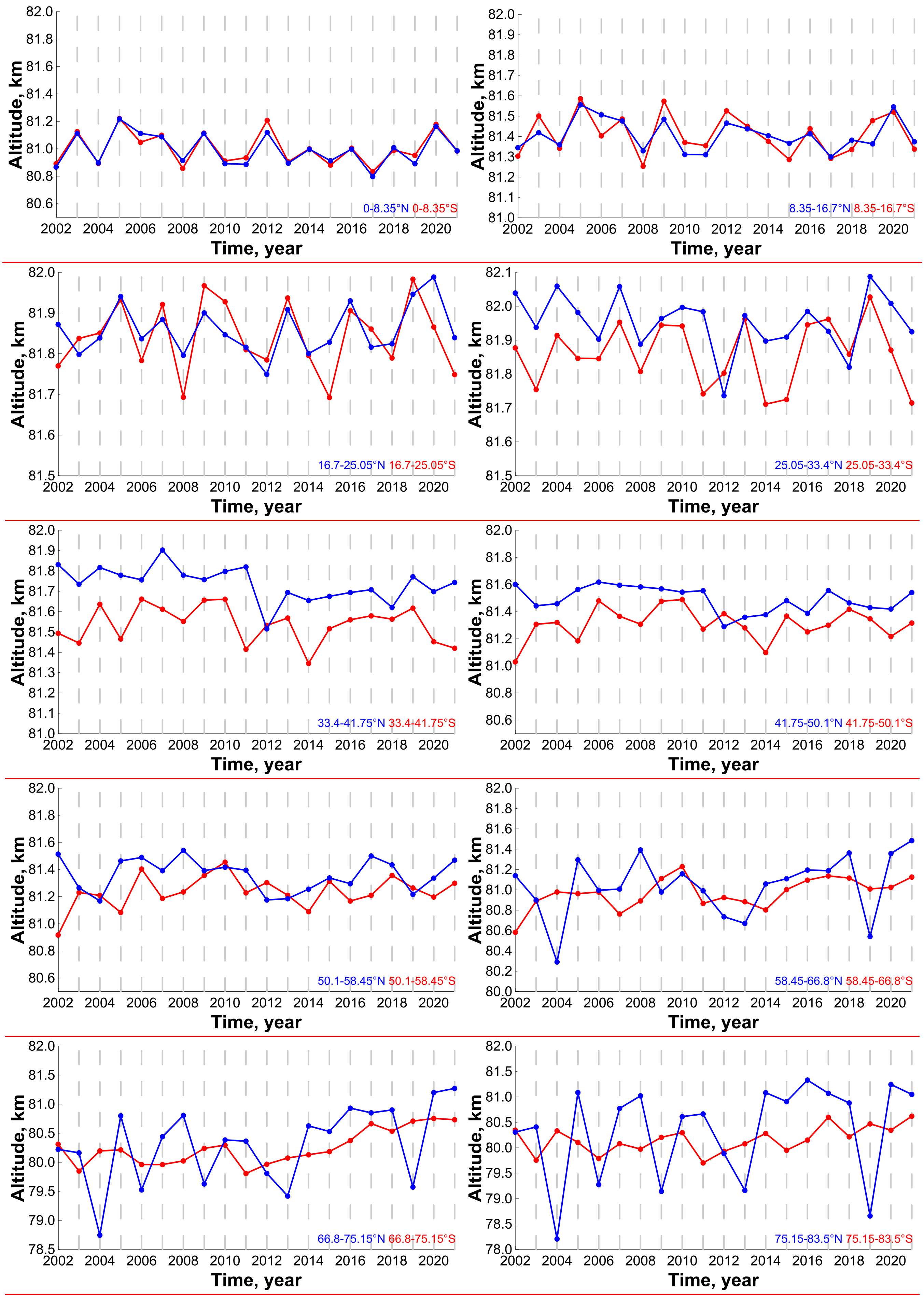
Altitude, km
Time, year
0-8.35°N 0-8.35°S
8.35-16.7°N 8.35-16.7°S
16.7-25.05°N 16.7-25.05°S
25.05-33.4°N 25.05-33.4°S
33.4-41.75°N 33.4-41.75°S
41.75-50.1°N 41.75-50.1°S
50.1-58.45°N 50.1-58.45°S
58.45-66.8°N 58.45-66.8°S
66.8-75.15°N 66.8-75.15°S
75.15-83.5°N 75.15-83.5°S

Figure 12. ~~Linear trend in $< z_{eq}^{pa} >$~~Time evolution of annually mean geometrical altitude $z_{eq}{}^{y}$ at different latitudes ~~derived from multiregression analysis.~~ .

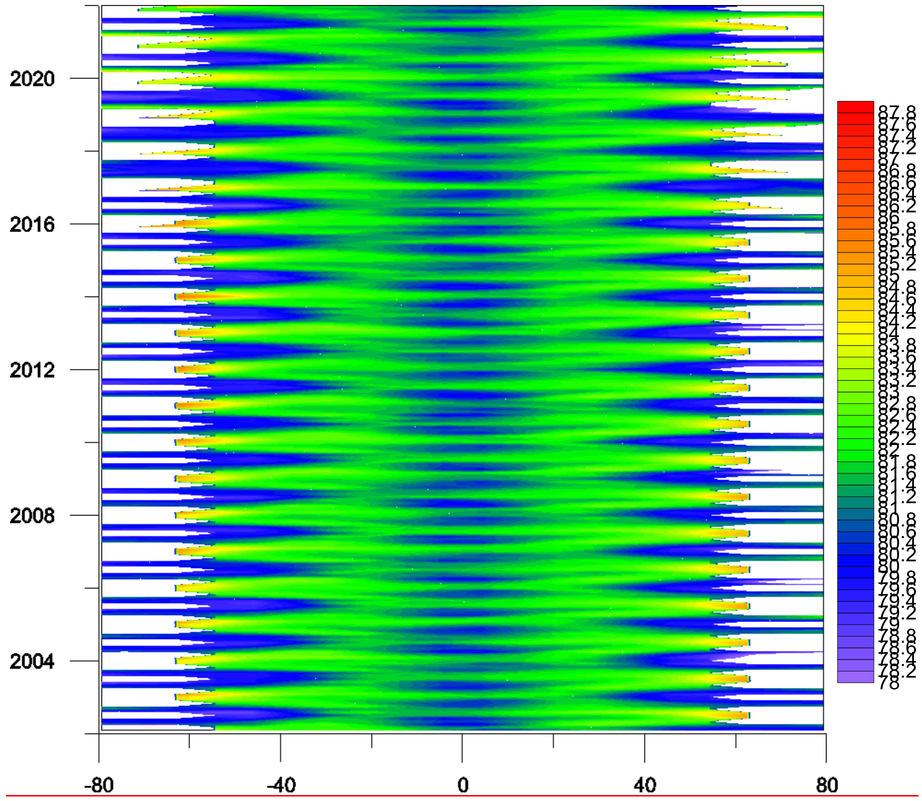

Figure 13. The space-time evolution of z_{eq}. White color indicates data gaps due to the satellite sensing geometry.

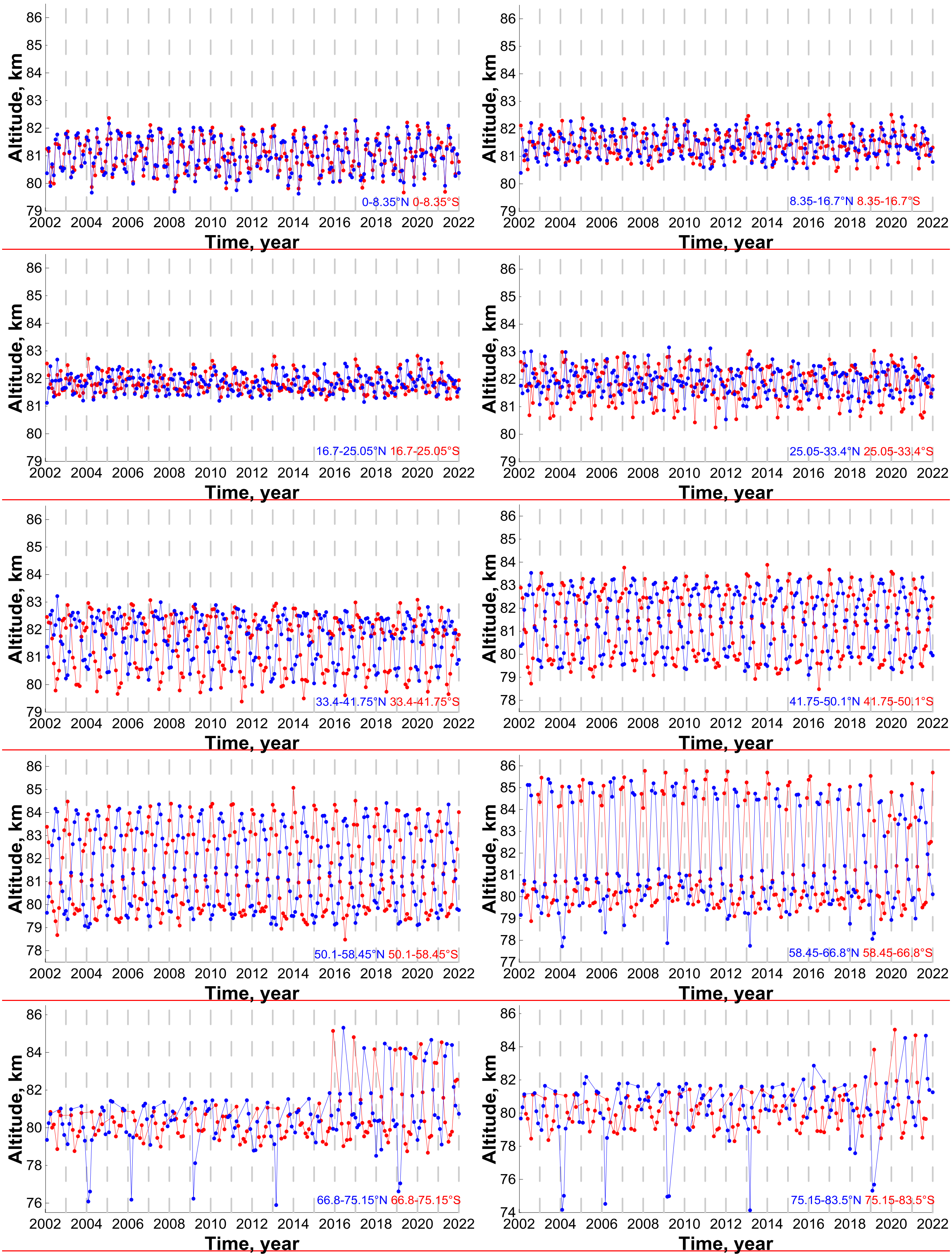

~~Figure 14. The time evolution of z_{eq} at different latitudes.~~

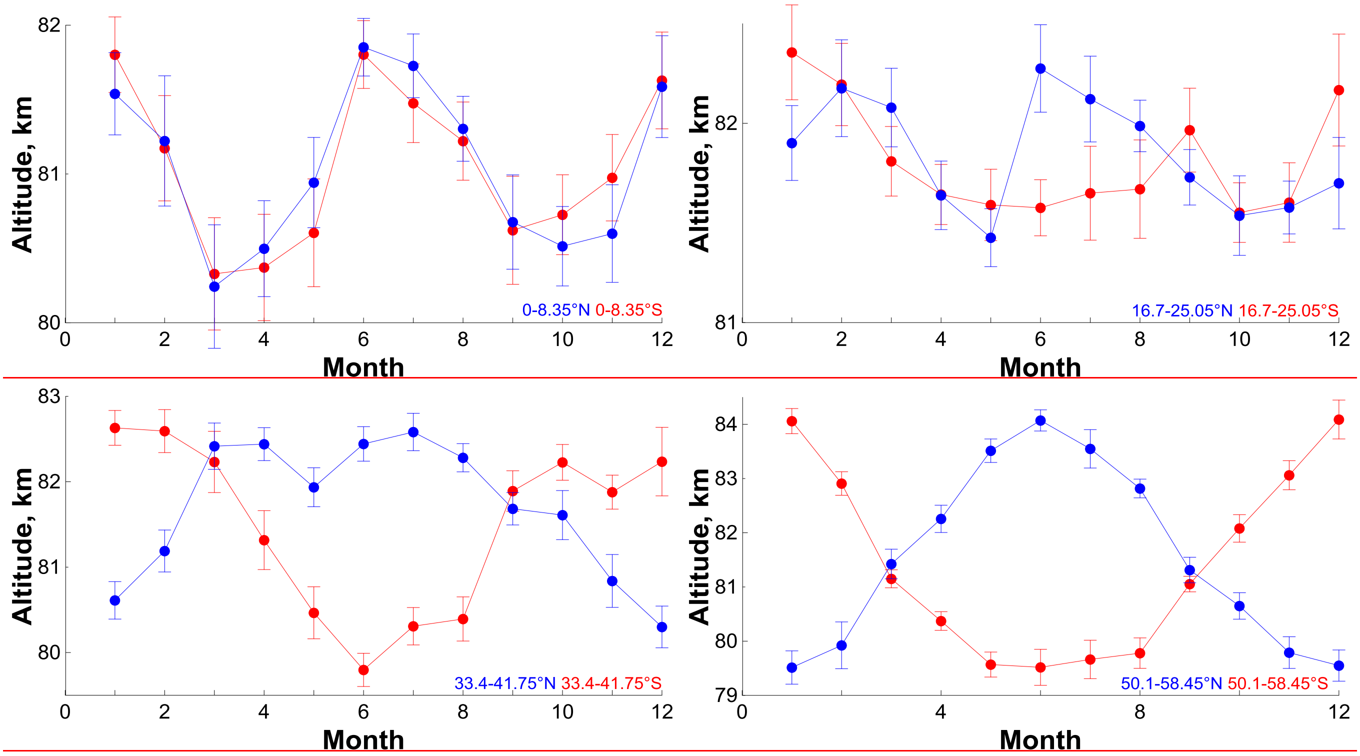

~~Figure 15. Average (for 2002-2021) annual cycle of z_{eq} at some latitudes.~~

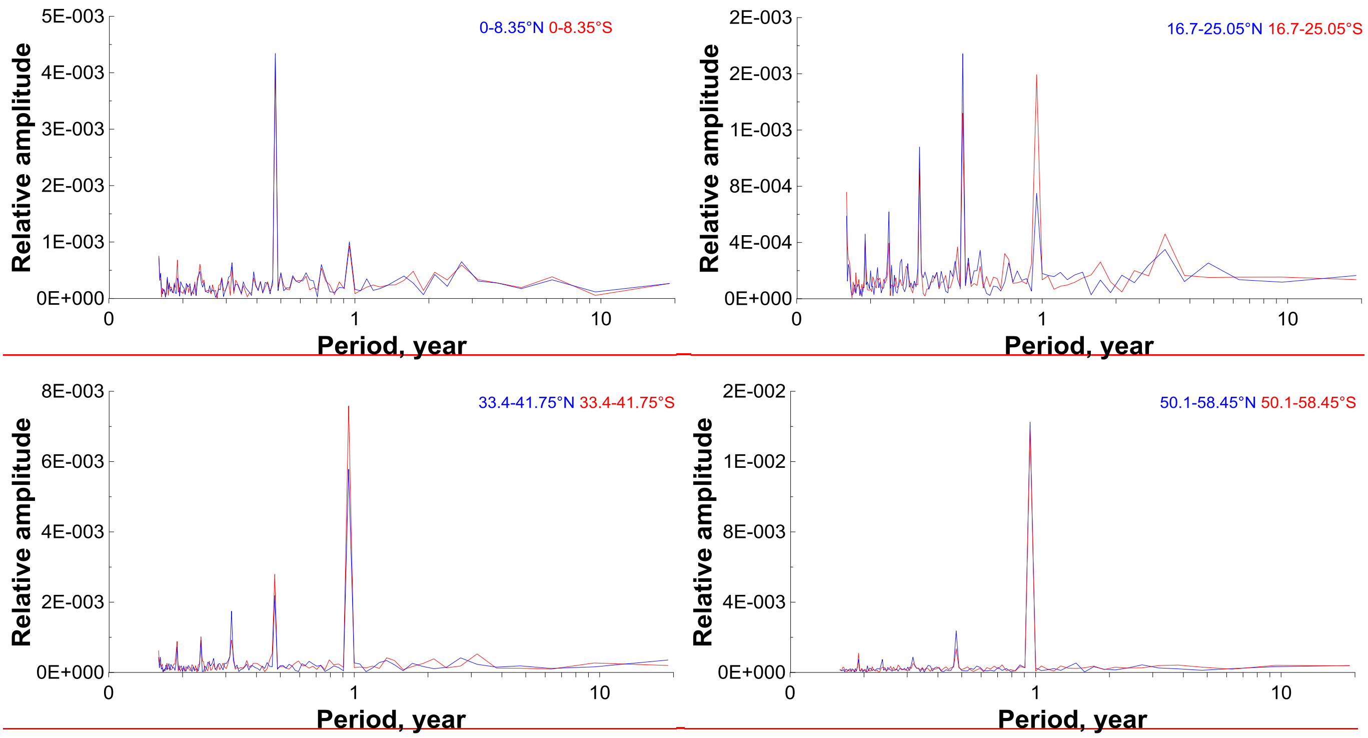

Figure 16. Fourier' spectra of z_{eq} time evolution at different latitudes. In each spectrum, the amplitudes of harmonics were normalized to corresponding zero harmonic.

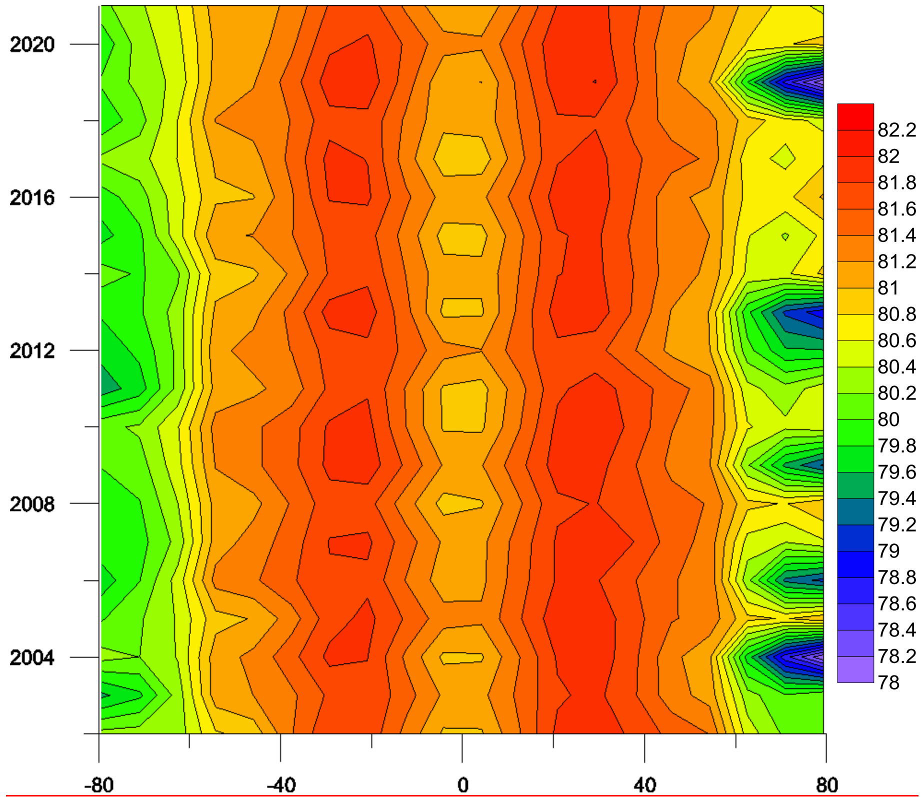

Figure 17. The latitude-time evolution of average annual z_{eq}.

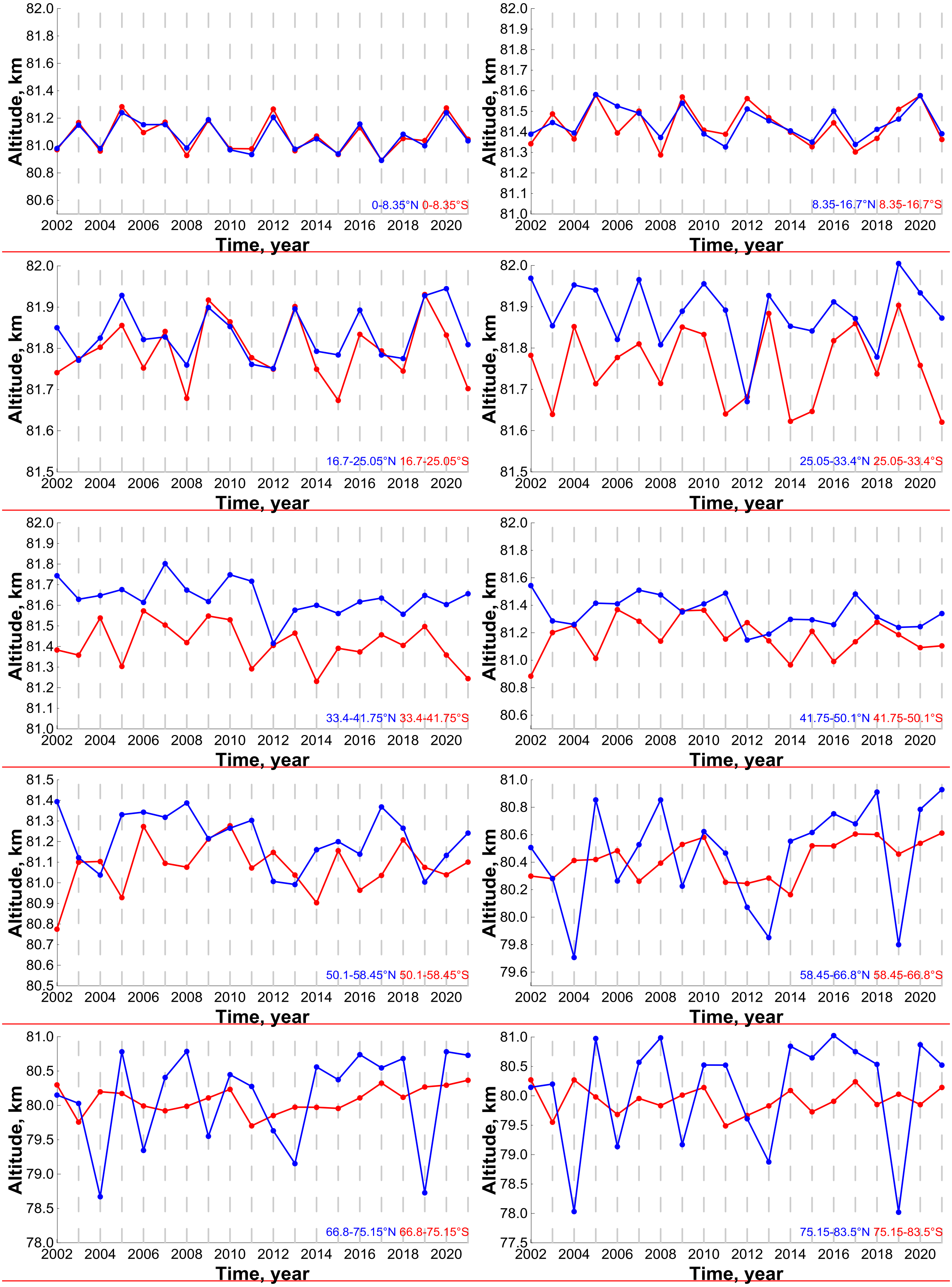

~~Figure 18. The time evolution of average annual z_{eq} ($< z_{eq} >$) at different latitudes.~~

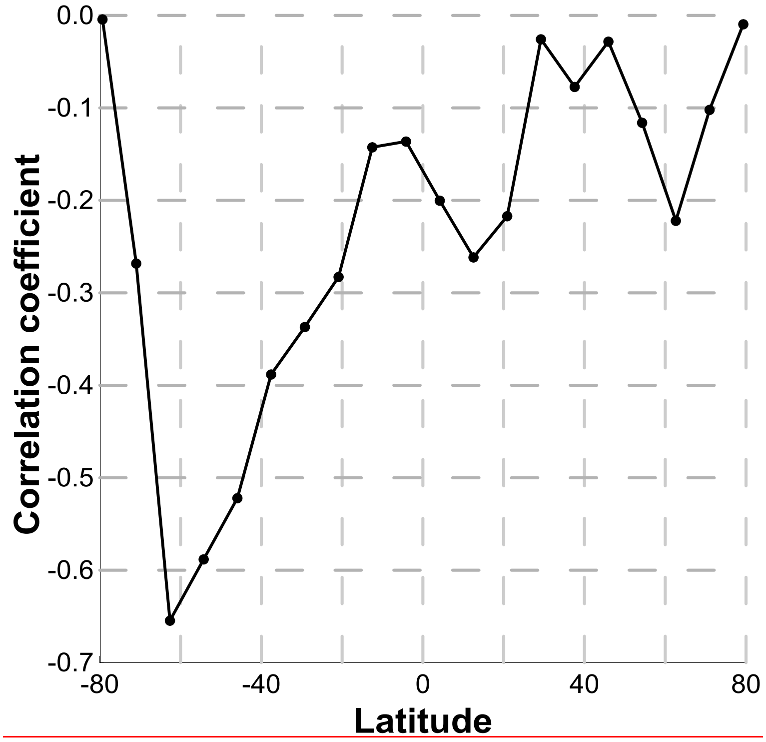

Figure 19. The correlation' coefficient of $< z_{eq} >$ with $F_{10.7}$ index at different latitudes.

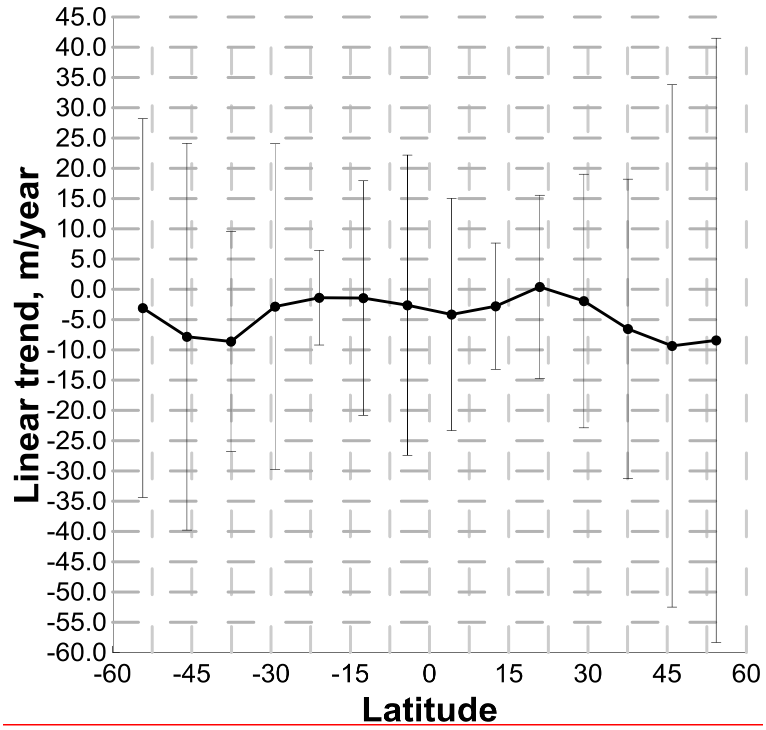

Figure 20. Linear trend in $< z_{eq} >$ at different latitudes derived from multiregression analysis.

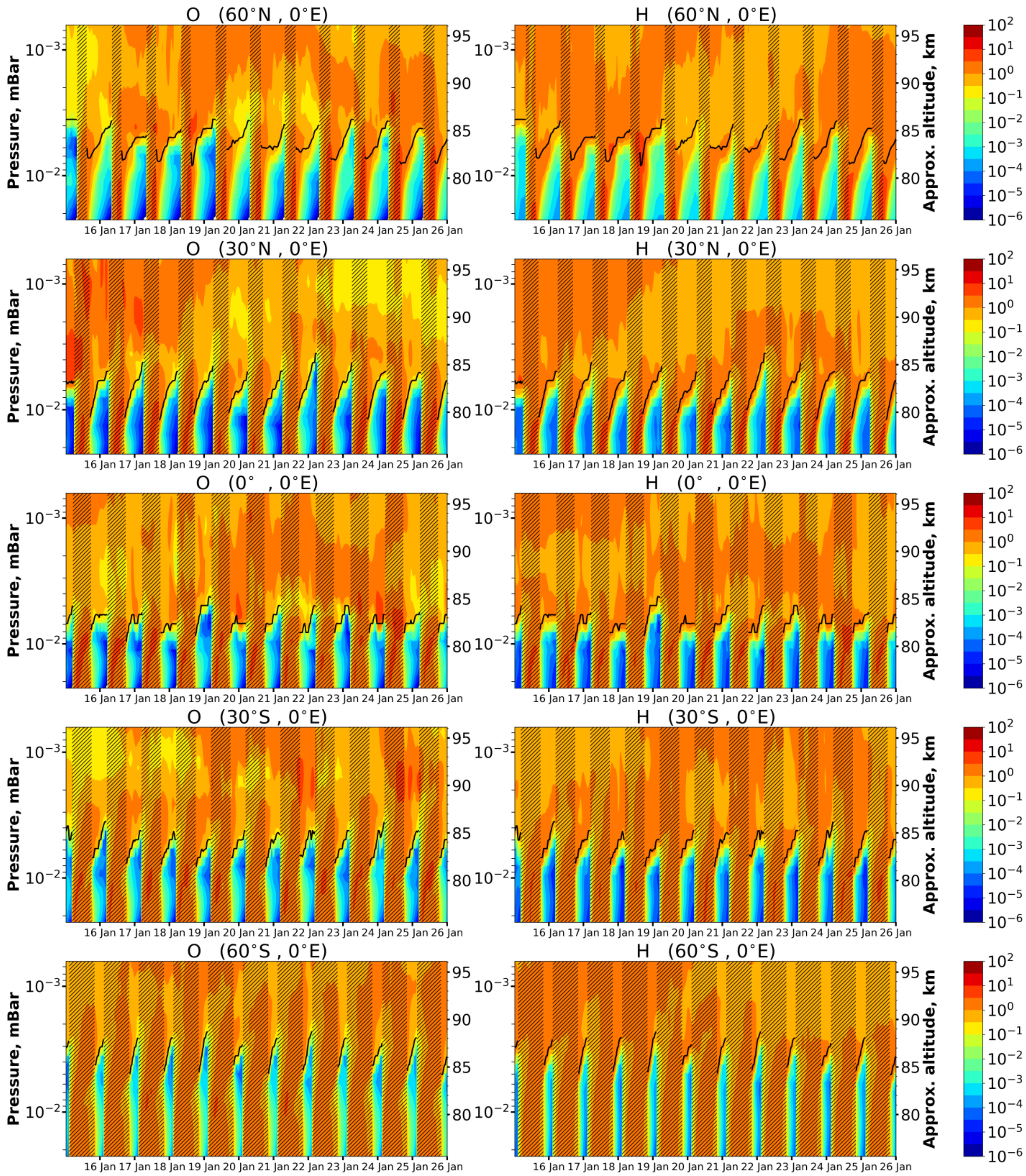

Figure 13. O and H time-height variations above different points in January 2017 calculated by 3D chemical transport model CMAM. Concentrations are normalized by mean daily values, correspondingly. Dark bars mark daytime, light bars mark nighttime. Black lines point the NOCE boundary altitude according to criterion (5) (Cr = 0.1).

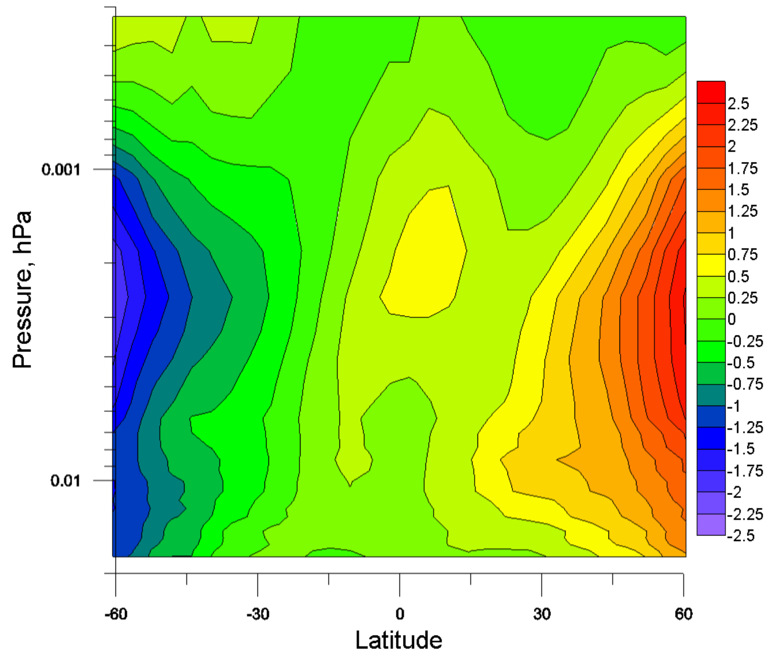

Figure 14. Logarithm of the ratio of $(O/H)_w$ and $(O/H)_s$ distributions obtained with the use of daytime seasonally mean distributions of O and H averaged in 2003-2015. $(O/H)_w$ was determined from the SABER data measured in December, January, and February. $(O/H)_s$ was determined from the SABER data measured in June, July, and August.